

# Global identification of solid waste methane super emitters using hyperspectral satellites

Xin Zhang<sup>a,1</sup>, Joannes D. Maasackers<sup>a</sup>, Javier Roger<sup>b</sup>, Luis Guanter<sup>b,c</sup>, Shubham Sharma<sup>a</sup>, Srijana Lama<sup>a</sup>, Paul Tol<sup>a</sup>, Daniel J. Varon<sup>d</sup>, Daniel H. Cusworth<sup>e</sup>, Katherine Howell<sup>e</sup>, Andrew K. Thorpe<sup>f</sup>, Philip G. Brodrick<sup>f</sup>, and Ilse Aben<sup>a,g</sup>

<sup>a</sup>SRON Netherlands Institute for Space Research, 2333 CA Leiden, The Netherlands;

<sup>b</sup>Research Institute of Water and Environmental Engineering, Universitat Politècnica de València, Valencia 46022, Spain;

<sup>c</sup>Environmental Defense Fund, 1083 HN Amsterdam, The Netherlands;

<sup>d</sup>School of Engineering and Applied Sciences, Harvard University, Cambridge, MA 02138;

<sup>e</sup>Carbon Mapper, Pasadena, CA 91105;

<sup>f</sup>Jet Propulsion Laboratory, California Institute of Technology, Pasadena, CA 91109;

<sup>g</sup>Department of Earth Sciences, Vrije Universiteit Amsterdam, 1081 HV Amsterdam, The Netherlands

<sup>1</sup>To whom correspondence should be addressed. Email: [xin.zhang@sron.nl](mailto:xin.zhang@sron.nl)

---

This is a non-peer-reviewed preprint submitted to EarthArXiv.

---



1 Global identification of solid waste methane super  
2 emitters using hyperspectral satellites

3 Xin Zhang<sup>1\*</sup>, Joannes D. Maasackers<sup>1</sup>, Javier Roger<sup>2</sup>,  
4 Luis Guanter<sup>2,3</sup>, Shubham Sharma<sup>1</sup>, Srijana Lama<sup>1</sup>, Paul Tol<sup>1</sup>,  
5 Daniel J. Varon<sup>4</sup>, Daniel H. Cusworth<sup>5</sup>, Katherine Howell<sup>5</sup>,  
6 Andrew K. Thorpe<sup>6</sup>, Philip G. Brodrick<sup>6</sup>, Ilse Aben<sup>1,7</sup>

7 <sup>1\*</sup>SRON Netherlands Institute for Space Research, Leiden, 2333 CA,  
8 The Netherlands.

9 <sup>2</sup>Research Institute of Water and Environmental Engineering,  
10 Universitat Politècnica de València, Valencia, 46022, Spain.

11 <sup>3</sup>Environmental Defense Fund, Amsterdam, 1083 HN, The Netherlands.

12 <sup>4</sup>School of Engineering and Applied Sciences, Harvard University,  
13 Cambridge, 02138, MA, USA.

14 <sup>5</sup>Carbon Mapper, Pasadena, 91105, CA, USA.

15 <sup>6</sup>Jet Propulsion Laboratory, California Institute of Technology,  
16 Pasadena, 91109, CA, USA.

17 <sup>7</sup>Department of Earth Sciences, Vrije Universiteit Amsterdam,  
18 Amsterdam, 1081 HV, The Netherlands.

19 \*Corresponding author(s). E-mail(s): [xin.zhang@sron.nl](mailto:xin.zhang@sron.nl);

20 **Abstract**

21 Solid waste is the third largest source of anthropogenic methane and miti-  
22 gating emissions is crucial for addressing climate change. We combine three  
23 high-resolution (30–60 m) hyperspectral satellite imagers (EMIT, EnMAP, and  
24 PRISMA) to quantify emissions from 38 strongly-emitting disposal sites across  
25 worldwide urban methane hotspots. The imagers give consistent emission esti-  
26 mates, with EMIT and EnMAP having better sensitivity than PRISMA. Total  
27 observed emissions add up to  $230 \pm 15 \text{ t h}^{-1}$ , representing 5% of reported global  
28 solid waste emissions. Our estimates exceed the facility-level Climate TRACE  
29 inventory by a factor of 1.8, while we only detect emissions from 9 of the

30 inventory’s 20 highest-emitting sites, highlighting the importance of facility-level  
31 information. Furthermore, multi-month observations reveal emission patterns  
32 potentially linked to facility operations. We estimate that these instruments could  
33 detect up to 60% of global landfill emissions, critically expanding on satellite  
34 instruments designed for methane and supporting emission mitigation.

35 **Keywords:** methane, hyperspectral, landfill, satellite, remote sensing

## 36 Introduction

37 Methane is a potent greenhouse gas with a global warming potential 27–30 times higher  
38 than carbon dioxide over a 100-year time scale [1]. Its relatively short atmospheric  
39 lifetime of about a decade makes reducing methane emissions critical for mitigat-  
40 ing near-term global warming. Anthropogenic activities account for ~60% of global  
41 methane emissions, with waste treatment as the third largest source (18%) after agri-  
42 culture and fossil fuel exploitation [2]. Moreover, the global waste generation could  
43 increase by ~60% from 2016 to 2050 [3], Waste methane emission reductions have  
44 become a priority for global climate action, as exemplified by the ‘Declaration on  
45 Reducing Methane from Organic Waste’ declaration introduced at the 29th UN Cli-  
46 mate Change Conference (COP29) [4]. In this declaration, countries responsible for  
47 over 50% of organic waste methane emissions committed to including reduction strate-  
48 gies in their climate plans. Several countries already announced specific plans and the  
49 Lowering Organic Waste Methane (LOW-Methane) initiative is focused on reducing  
50 annual global waste methane emissions by one million metric tonnes a year by 2030  
51 and unlocking 10 billion dollars in funding to achieve this goal [5].

52 However, accurately quantifying landfill methane emissions remains challenging,  
53 with substantial uncertainties in both site-specific and global estimates [6–9]. While  
54 traditional approaches rely on modeling and limited aircraft measurements [6, 10–13],  
55 space-borne monitoring offers a way to improve emission quantification. A 2022 study  
56 [14] demonstrated the application of GHGSat observations to quantify emissions from

57 four landfills, including one in Buenos Aires that contributed 50% of the city’s methane  
58 emissions. However, facility-scale coverage by satellites designed to observe methane is  
59 currently limited. Here we therefore evaluate the potential of using alternative imaging  
60 spectrometers to extend that coverage and quantify emissions from individual landfills.

61 The TROPOspheric Monitoring Instrument (TROPOMI) [15, 16] has been used  
62 for monitoring regional methane emissions [17, 18] and detecting urban super-emitters  
63 [14, 19]. However, its spatial resolution ( $5.5 \times 7 \text{ km}^2$  at nadir) typically cannot sepa-  
64 rate landfill emissions from other city emissions [14]. Currently, the only operational  
65 spaceborne instruments specifically designed to measure methane at facility-level are  
66 the commercial satellites from the GHGSat constellation [20, 21]. A small fraction of  
67 the GHGSat data are publicly available and individual observations only cover an area  
68 of  $\sim 12 \times 15 \text{ km}^2$ . Recent studies highlight the use of public multispectral [22–24] and  
69 hyperspectral imagers (HSIs) [25–27] for detecting large point sources, primarily from  
70 the oil/gas industry. HSIs, similar to the next generation Airborne Visible/Infrared  
71 Imaging Spectrometer (AVIRIS-NG) [8, 28], are not designed for methane detection  
72 but offer relatively high methane sensitivity through hundreds of narrow spectral  
73 bands. Starting with PRecursore IperSpettrale della Missione Applicativa (PRISMA)  
74 [29, 30], HSIs have been verified to be capable of detecting plumes down to 300–500 kg  
75  $\text{h}^{-1}$  [31, 32] in favorable conditions such as bright homogeneous desert scenes, outper-  
76 forming multispectral sensors such as Sentinel-2 [22–24]. Thus, HSIs are particularly  
77 promising for detecting landfill methane emissions, which are more diffuse than those  
78 from oil/gas operations and occur over more complex terrain.

79 Previous studies have demonstrated the potential of HSIs in detecting landfill  
80 methane emissions. The Environmental Mapping and Analysis Program (EnMAP)  
81 [33, 34] has been used to detect emissions from the Ghazipur and Okhla landfills in  
82 Delhi [27], while Earth Surface Mineral Dust Source Investigation (EMIT) [33, 34] has  
83 been used to detect emissions from 11 different landfills around the world [26]. To assist

84 in mitigating global landfills, it is crucial to construct a comprehensive global land-  
85 fill emission dataset. Here, we integrate TROPOMI and three HSIs (EMIT, EnMAP,  
86 and PRISMA) to identify, quantify, and monitor high-emitting landfills worldwide.  
87 As part of the analysis, we compare the performance of all HSIs and examine the  
88 impact of wind speed uncertainty on the emission quantification. We also compare our  
89 results against existing emission inventories. Our analysis assesses hyperspectral imag-  
90 ing’s potential to monitor global landfill methane, expanding upon current satellite  
91 capabilities designed for methane observation.

## 92 **Results**

### 93 **Landfill methane hot spots**

94 Figure 1 shows the overview of urban and landfill methane hot spots detected by  
95 TROPOMI and HSIs, along with examples of typical methane plumes observed by  
96 HSIs. Using 2020–2023 TROPOMI data, we identified persistent global urban methane  
97 hot spots based on plume detections and analysis of long-term averages (see *Methods*)  
98 [14, 19]. Among all hot spots, 58 are potentially associated with landfill emissions given  
99 their source locations, although they may also include contributions from other urban  
100 sources. We evaluate 46 landfills within these TROPOMI hot spots using EMIT and  
101 EnMAP, while the remaining 12 lack observations. PRISMA has clear-sky observations  
102 for 49 landfills (Supplementary Fig. S8) but only detects plumes from 4 due to its  
103 lower methane sensitivity, caused by lower signal-to-noise ratio (SNR) and spectral  
104 resolution (see *Methods*).

105 Overall, the HSI data reveal detectable plumes from 38 landfills: 25 within 15 km of  
106 TROPOMI hot spots and 13 at nearby locations (Fig. 1). EMIT, with its wider scene  
107 coverage, observes all 38 landfills in clear-sky conditions and detects plumes from 36  
108 (Supplementary Fig. S8). EnMAP shows a comparable capability, detecting plumes  
109 from 16 out of 18 observed landfills, while PRISMA, due to its lower sensitivity, only

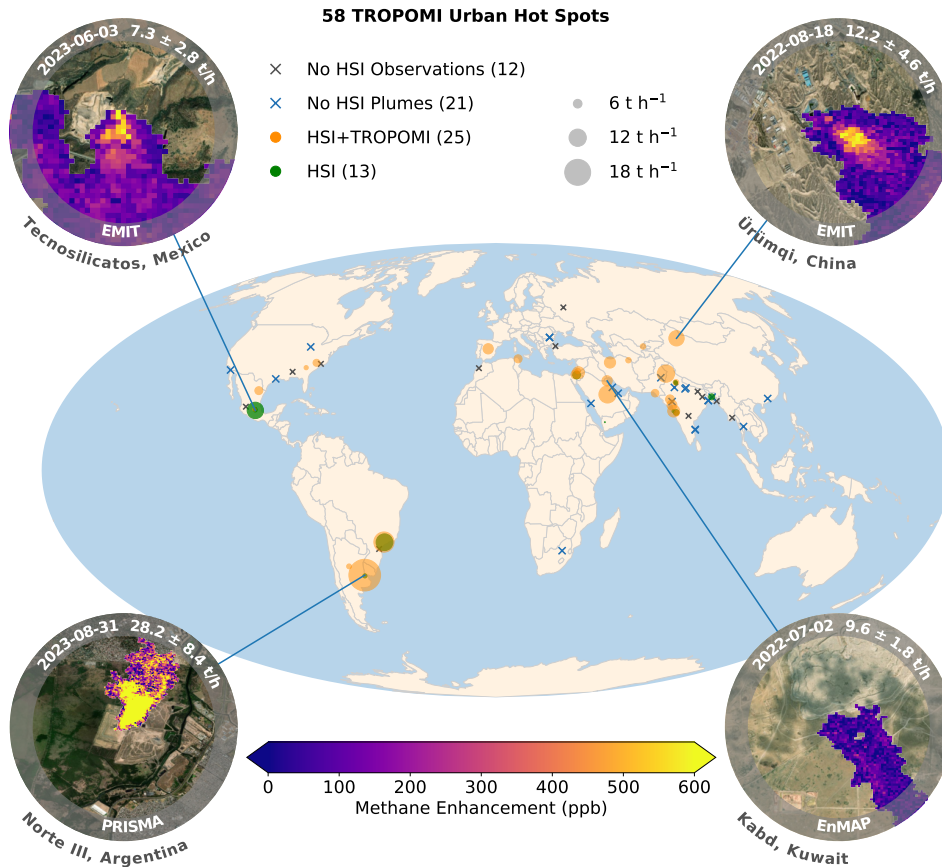


**Fig. 1** Urban hot spots detected by TROPOMI (2020–2023) and landfill emissions detected at those hot spots using hyperspectral imagers (HSIs) including EMIT, EnMAP, and PRISMA. Gray crosses indicate TROPOMI hot spots without clear-sky HSI data, blue crosses show hot spots with clear-sky HSI observations without detected plumes, orange circles show TROPOMI hot spots with HSI plumes, and green circles indicate plumes detected by HSIs slightly away from the TROPOMI hot spots. The 'No HSI Observations' group excludes PRISMA due to its lower methane sensitivity. Insets show typical landfill plumes with detection date, emission rate, uncertainty, landfill/country name, and instrument. Background imagery comes from Esri World Imagery [35]. Supplementary Fig. S7 shows a zoomed-in view of landfill emissions across India.

110 detects plumes at 4 out of 32 observed sites. Among the 38 landfills with detected  
 111 plumes, 29 are observed at least twice, with 10 having 8–14 plume detections, facil-  
 112 itating emission time series analysis (see *Emission Variations*). The total number of  
 113 plumes detected by each HSI is as follows: EMIT observes 132 plumes, EnMAP 38,  
 114 and PRISMA 10 (Supplementary Fig. S9).

115 This highlights the potential of EMIT and EnMAP in identifying landfill emission  
116 sources, whereas PRISMA is constrained by a higher detection threshold. When cal-  
117 culating mean emission rates, we use different approaches for each instrument. For  
118 EnMAP and EMIT, we conservatively assume zero emission when clear-sky overpasses  
119 yield no detected plumes. In the case of PRISMA, owing to its lower sensitivity, we  
120 only include instances where plumes are detected in our emission rate calculations.

## 121 **Landfill methane emission rates**

122 A commonly used data-driven approach for methane retrieval from HSIs involves a  
123 matched filter algorithm that maximizes the signal-to-background ratio by identifying  
124 pixels exhibiting the strongest correlation with methane’s absorption spectrum. We  
125 improve the traditional matched filter to retrieve methane enhancements using Level 1  
126 radiance data and to estimate emission rates through the integrated mass enhancement  
127 (IME) method, specifically calibrated for each instrument (see *Methods*). The reported  
128 uncertainties include contributions from wind speed error, retrieval random error,  
129 and IME calibration error (Supplementary Section 1). We validate our methodology  
130 using two controlled releases (Supplementary Section 2), one for PRISMA (October  
131 21, 2021) and one for EnMAP (November 16, 2022). Both controlled releases show  
132 our satellite estimates agree with the controlled flow rates within their uncertainties  
133 (Supplementary Fig. S2). While these validations are performed using point-source  
134 controlled releases, we expect controlled releases simulating more dispersed emissions  
135 from landfills will become available in the near-future. While the overpasses for dif-  
136 ferent HSIs typically vary in timing over the same landfill, the average magnitudes of  
137 emission rates between EnMAP and EMIT are consistent (slope= $1.21 \pm 0.17$ ,  $r=0.84$ ,  
138 Supplementary Fig. S10a). We therefore use data from both instruments together for  
139 the remainder of this study. PRISMA’s emission rate estimates for two landfills are

140 consistent with those from EMIT and EnMAP in the same year (Supplementary Fig.  
141 [S10b](#)).

142 Figure 2 shows our methane emission rates for 38 landfills across 17 countries with  
143 the lowest rate being  $\sim 1 \text{ t h}^{-1}$ . The sum of mean emission rates across sites is  $230$   
144  $\pm 15 \text{ t h}^{-1}$ , with most of the observed high-emitting landfills located at hot spots in  
145 India, Argentina, Brazil, and Mexico. India stands out with the highest total of  $41.4$   
146  $\pm 5.0 \text{ t h}^{-1}$  from 10 landfills. Argentina follows at  $28.1 \pm 6.6 \text{ t h}^{-1}$ , primarily driven  
147 by the Norte III landfill in Buenos Aires, showing the highest emission rate among all  
148 observed landfills at  $22.0 \pm 6.4 \text{ t h}^{-1}$ . Brazil has a similar emission of  $25.6 \pm 6.3 \text{ t}$   
149  $\text{h}^{-1}$ , with the Caieiras ( $14.0 \pm 4.8 \text{ t h}^{-1}$ ) and Pedreira ( $11.5 \pm 4.0 \text{ t h}^{-1}$ ) landfills in  
150 Sao Paulo strongly contributing to this total. These three large-emitting landfills in  
151 Buenos Aires and Sao Paulo account for 20% of the total quantified landfill methane  
152 emissions. Mexico ranks fourth at  $23.7 \pm 5.3 \text{ t h}^{-1}$ , half of which comes from the  
153 Tecnosilicatos landfill in Mexico City.

154 Among the remaining 13 countries, each with only 1 to 2 observed landfills, six  
155 have a total emission rate ranging from 10 to  $17 \text{ t h}^{-1}$ . This can be attributed to the  
156 presence of large emitting landfills, such as the Lakhodair landfill ( $12.0 \pm 4.2 \text{ t h}^{-1}$ )  
157 in Pakistan, the Riyadh landfill ( $12.0 \pm 3.4 \text{ t h}^{-1}$ ) in Saudi Arabia, the Ürümqi land-  
158 fill ( $10.7 \pm 4.4 \text{ t h}^{-1}$ ) in China, the Ghabawi landfill ( $8.4 \pm 2.4 \text{ t h}^{-1}$ ) in Jordan,  
159 and the Tehran landfill ( $7.8 \pm 2.8 \text{ t h}^{-1}$ ) in Iran. The cumulative distribution reveals  
160 that for this set of 38 landfills, the top 20% highest emitters contribute 46% of the  
161 inferred total emission (Supplementary Fig. [S11a](#)). This highlights the importance of  
162 detecting and mitigating high methane-emitting landfills. Due to variations in back-  
163 ground noise levels, wind speed, and potential methane emission variability, landfill  
164 methane plumes are sometimes detected by one HSI and missed by another (crosses  
165 in Fig. 2). This emphasizes the value of combining multiple HSIs to monitor landfill



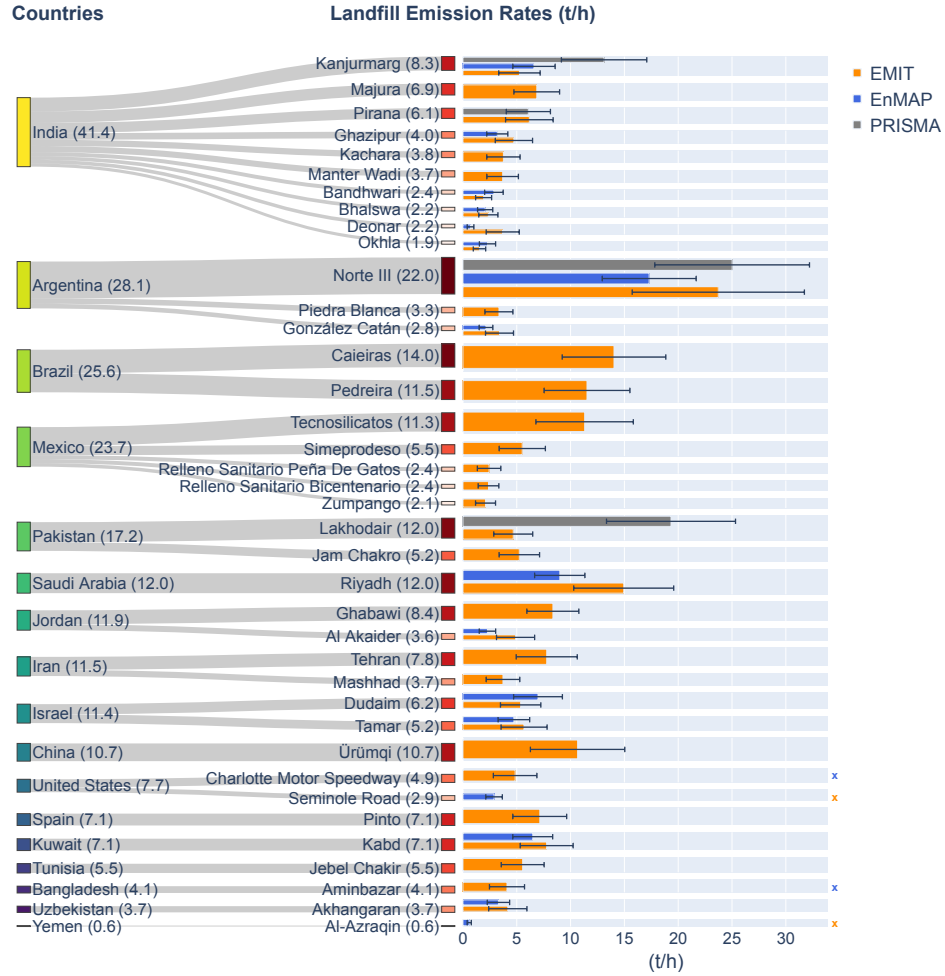


**Fig. 2** Sankey plot for the landfill emissions estimated using hyperspectral imagers (HSIs). Box heights are proportional to emission rates ( $t h^{-1}$ ), with values in brackets. Colored bars show estimates from different instruments, with uncertainties in black. Crosses on the right indicate EMIT or EnMAP overpasses without detected methane plumes. Non-detections with PRISMA are not depicted, given PRISMA's lower sensitivity. More details are given in Supplementary Tables S1 and S2.

166 emissions. However, in most cases, both EnMAP and EMIT detect emissions from spe-  
 167 cific landfills, thereby increasing the observation opportunities for landfill emissions.  
 168 For cases with a single detected plume (Supplementary Fig. S9), estimates may be  
 169 affected by potential offsets. Future studies with more data will be crucial for refining  
 170 these constraints.

## 171 Comparison with observations and inventories

172 First, we compare our HSI estimates with recent satellite, aircraft, and ground-based  
173 observations (Fig. 3a) [14, 26, 36, 37]. For eight of the observed landfills, there are  
174 estimates from earlier studies. Our HSI results show good agreement with these esti-  
175 mates (slope= $1.31 \pm 0.14$ ,  $r=0.97$ , Fig. 3a), though the number of data points is limited  
176 (Supplementary Table S3). We then compare our facility-level methane emission esti-  
177 mates with the Climate Tracking Real-time Atmospheric Carbon Emissions (Climate  
178 TRACE) dataset, which models emissions using multiple waste datasets (see *Methods*).  
179 We find that the Climate TRACE dataset generally underestimates landfill emissions  
180 compared to HSI for the 26 landfills with overlapping estimates (Supplementary Fig.  
181 3a and Table S4). Based on the HSI measurements, total methane emissions ( $141 \pm$   
182  $11 \text{ t h}^{-1}$ ) from these landfills are 1.8 times higher than the estimates in the Climate  
183 TRACE inventory. Some of the data used in the Climate Trace inventory may be  
184 outdated. For example, the Norte III landfill data from the 2013 Waste Atlas reports  
185 emissions of  $3.3 \text{ t h}^{-1}$ , significantly lower than our estimate of  $22.0 \pm 6.4 \text{ t h}^{-1}$ . Con-  
186 sidering only the 2021 and 2022 Climate Trace data for 15 landfills, our estimates  
187 are only 1.3 times higher. However, comparing individual facilities, the median ratio  
188 between our estimates and the Climate Trace data is still 4.7, exceeding the 1.6 ratio  
189 found in comparisons with previous studies. Therefore, the differences appear to be  
190 related not only to up-to-date information on landfill activities but also to appropriate  
191 emission factors representative of operations at the different landfills.

192 In addition to the landfills at hot spots, we then focus on Climate TRACE’s top  
193 20 highest emitting landfills (Fig. 3b and Supplementary Table S5). HSIs overpass all  
194 20 landfills, but only detect plumes from 9 still-active landfills, while the remaining 11  
195 appear inactive based on vegetation covering the landfill as seen in Sentinel-2 imagery  
196 (Supplementary Fig. S12). Among nine active landfills, our estimates are consistent  
197 with Climate TRACE for four but are 48~71% lower for the other five. For two of these

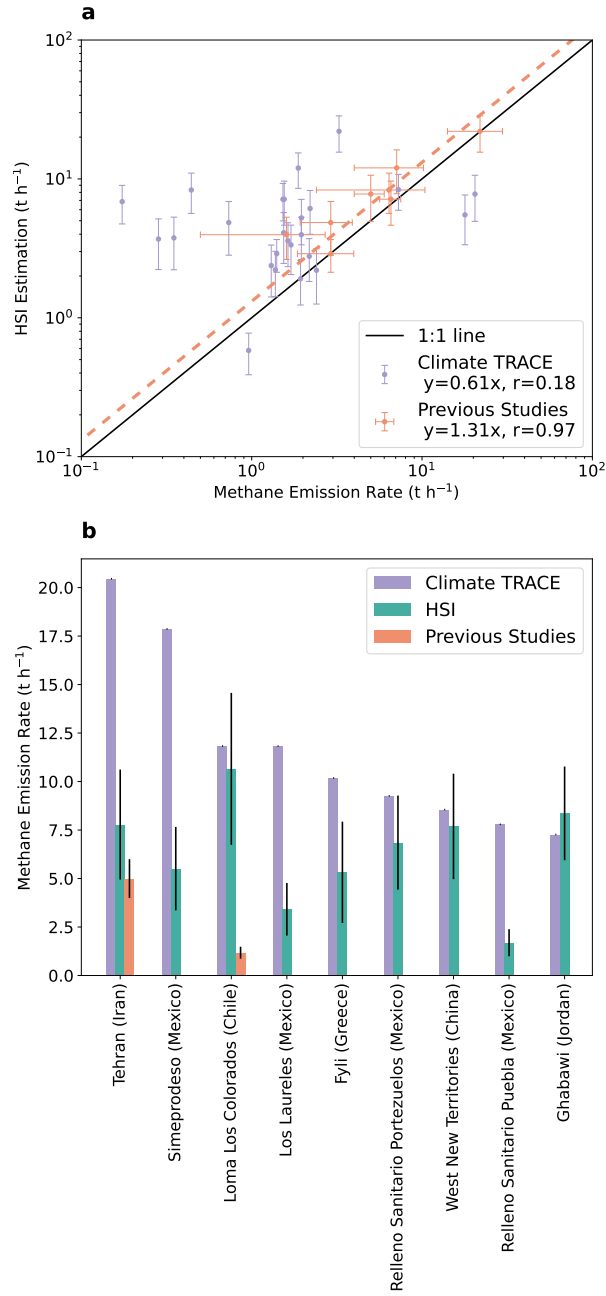


**Fig. 3** Comparison of methane emission rates from hyperspectral imager (HSI) observations, the Climate TRACE inventory, and observational estimates from the literature for (a) landfills mapped in Fig. 1, and (b) the top 20 methane-emitting landfills in the Climate TRACE dataset (see Supplementary Table S3, S4, and S5 for details). The regression coefficients are calculated using orthogonal distance regression. The Pearson correlation coefficients are 0.18 between HSI and Climate TRACE, and 0.97 between HSI and previous studies.

198 landfills (Tehran and Loma Los Colorados), additional observational estimates are  
199 available in the literature. Our estimate for the Tehran landfill agrees with an earlier  
200 EMIT analysis [26]. However, four Airborne Visible InfraRed Imaging Spectrometer  
201 – Next Generation (AVIRIS-NG) observations of the Loma Los Colorados landfill in  
202 January and February 2023 reported emissions of  $1.2 \pm 0.3 \text{ t h}^{-1}$  [37], which is 89%  
203 lower than our EMIT-based estimate for January and 90% lower than the Climate  
204 TRACE estimate. These results show that differences between facility-level observa-  
205 tions and bottom-up estimates can go both ways and that there may be substantial  
206 temporal variability in emissions. Some variability may also be due to differences in  
207 quantification algorithms applied to remote sensing datasets. Using the same EMIT  
208 observations, we compare methane emissions across 36 landfills using Carbon Mapper’s  
209 IME-fetch method (Supplementary Section 4). We find that some significant variabil-  
210 ity can be traced to quantification uncertainties, particularly in plume masking. This  
211 variability can be reproduced using large-eddy simulations. Despite these variations,  
212 the overall emission results remain consistent across quantification algorithms for most  
213 landfills in this study.

214 In addition to facility-level comparisons, we evaluate how our HSI estimates com-  
215 pare to solid waste methane emission inventories at the city scale from the Waste  
216 Methane Assessment Platform (WasteMAP). Of the 15 cities included in both the  
217 WasteMAP platform and our analysis, accounting for uncertainties, only two have  
218 higher emissions in WasteMAP than our summed HSI landfill estimates (Supplemen-  
219 tary Fig. S13a and Table S6). HSI emissions from the Pinto (Spain), Simeprodeso  
220 (Mexico), and Jebel Chakir (Tunisia) landfills alone are 16~27 times higher than total  
221 city emissions for Madrid, Monterrey, and Tunis, respectively. The mean ratio of our  
222 HSI-derived landfill emissions to city totals is 6.3. One reason for this high ratio may  
223 be that these landfills service a larger area than the cities they are within. Meanwhile,

224 this ratio is likely underestimated because emissions from many smaller landfills are  
225 undetected by HSI.

226 At the country level, Climate TRACE solid waste emissions generally exceed the  
227 sum of our HSI landfill emissions (Supplementary Fig. S13b and Table S7). This  
228 difference arises because HSI measurements typically only cover a small fraction of  
229 the landfills included in the Climate TRACE data, while Climate TRACE’s country-  
230 level inventory considers all solid waste emissions. However, Climate TRACE’s total  
231 facility-level emissions are 47% lower than HSI estimates in six countries, while the  
232 remaining countries show emissions that are either higher than or comparable to  
233 HSI estimates (Supplementary Fig. S13b). These findings highlight the importance of  
234 evaluating and improving emission inventories across scales using observations, partic-  
235 ularly accounting for strongly-emitting landfills that may be underestimated in current  
236 inventories.

### 237 **Emission variations**

238 The multiple overpasses of HSIs enable us to examine the spatial and temporal vari-  
239 ations in emissions (Supplementary Fig. S14). Specifically, the Ghabawi landfill in  
240 Jordan has a total of 14 EMIT observations, with measurements taken every 1–2  
241 months throughout 2023 (Fig. 4). Between February and April 2023, the emission rate  
242 increased from  $5.1 \pm 1.7 \text{ t h}^{-1}$  to  $17.2 \pm 4.3 \text{ t h}^{-1}$ . Then it decreased to  $3.9 \pm 1.8 \text{ t}$   
243  $\text{h}^{-1}$  in September, before increasing again to  $9.3 \pm 2.1 \text{ t h}^{-1}$  in December.

244 The variation in emission rates is not correlated with the wind speed magnitude.  
245 It is also seen when using an alternate wind product and quantification method to  
246 calculate emission rates (Supplementary Section 1, Fig. S15 and S16). We then track  
247 waste disposal activities using Sentinel-2 RGB images captured within 3 days of each  
248 EMIT overpass (Fig. 4 a–c). These images show a shift in the plume source location  
249 from the northern cell to a newly established southern cell. The year-round Sentinel-2

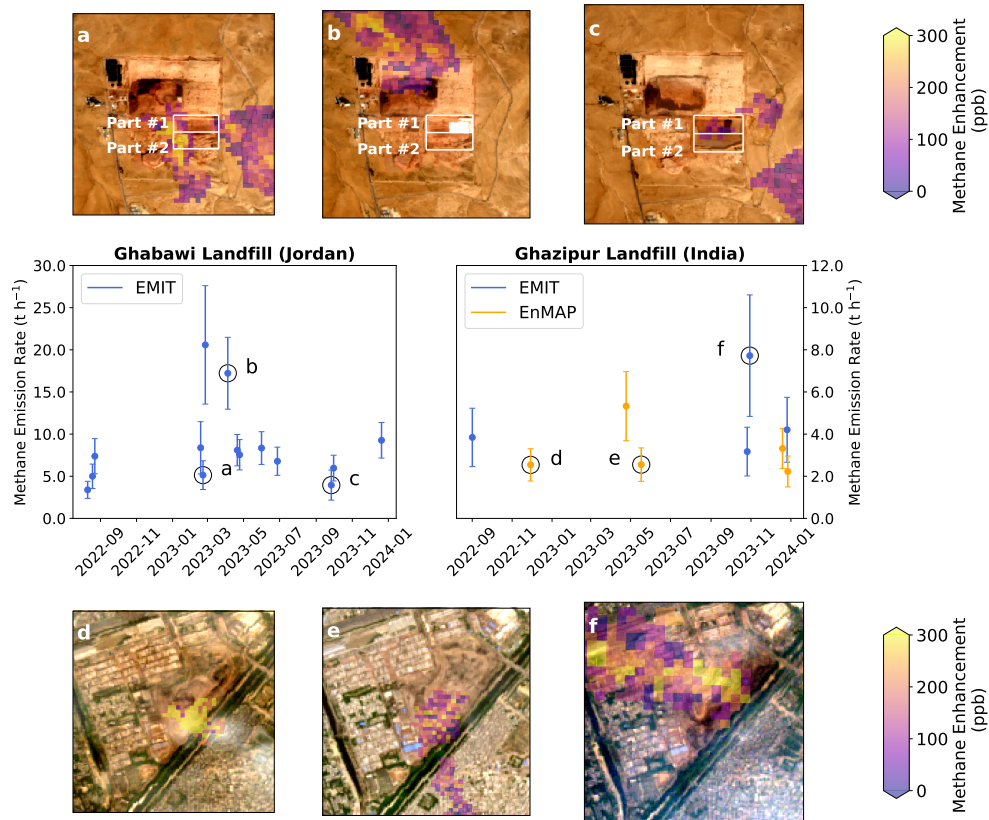


**Fig. 4** Time series of methane emissions from the Ghabawi (Jordan) and Ghazipur (India) landfills as derived using EMIT and EnMAP data. The complete Sentinel-2 RGB time series for 2023 are available as Movies S1 and S2. The points marked with letters a–f correspond to the insets labeled with matching letters in their upper left corners. (a–c) Methane plumes observed at the Ghabawi landfill shown over Sentinel-2 images [38] captured within 3 days of the EMIT overpass: (a) 21 February 2023, (b) 4 April 2023, (c) 26 September 2023. The white rectangles highlight two sections in the newly constructed southern section. (d–f) Similar observations for the Ghazipur landfill: (d) 29 November 2022, (e) 17 May 2023, (f) 30 October 2023.

250 images (Supplementary Fig. S17 and Movie S1) show the construction process of the  
 251 southern cell was divided into two phases: March to June (part #1, Fig. 4b) and June  
 252 to September (part #2, Fig. 4c), while waste deposition in the cell began in August.  
 253 Although the spike in methane emission rates coincides with the active construction of  
 254 part #1 in April, the plume’s source is not located within this newly constructed area.  
 255 Instead, it originates from waste deposited in earlier phases of the landfill (Fig. 4b).  
 256 These observations align with previous studies highlighting how variability in landfill

257 emissions is heavily influenced by operational procedures, such as the choice of cover  
258 material or alterations in landfill infrastructure, alongside local weather conditions  
259 [12, 39]. Retrieval artifacts can also cause minor variations due to the confounding  
260 influence of the landfill’s surface materials in the methane retrieval spectral window  
261 (2100–2450 nm).

262     Given the sparse temporal sampling of landfills by individual HSI instruments,  
263 combining observations from all available HSI sensors is valuable for exploring emis-  
264 sion time series. The Ghazipur landfill in Delhi, India, is an illustrative example (Fig.  
265 4 d–f). Despite infrequent revisits, we find that the emission source shifted from the  
266 southern section to the northeast, corresponding to increasing activity in the north-  
267 eastern section, as shown by the Sentinel-2 images (Supplementary Fig. S18 and  
268 Movie S2). The combined analysis of HSI data and satellite imagery demonstrates  
269 the capability to capture both spatial and temporal changes in landfill operations and  
270 associated methane emissions. When more HSI observations become available in the  
271 future, they will help us estimate baseline methane emissions more accurately and  
272 improve long-term projections of landfill methane emissions.

## 273 **Discussion**

274 We have analyzed global methane emissions from landfills by integrating observations  
275 from TROPOMI and HSIs. TROPOMI first identifies urban hot spots indicative of  
276 potentially large landfill methane emissions, which are then targeted by analysis of  
277 HSIs. Our findings reveal differences with current landfill emission inventories, high-  
278 lighting the critical need for observation-based updates to account for super-emitting  
279 sites. Furthermore, measurements from different HSIs can be used to monitor emissions  
280 over time at any specific site and enable exploring emission variability resulting from  
281 operational procedures. This synergistic use of spaceborne sensors establishes a robust  
282 framework for continuous global monitoring of landfill methane emissions. Given that

283 80% of landfill methane emissions could be mitigated through existing technological  
284 solutions [40, 41], our publicly available spaceborne methane emission products can  
285 assist efforts to monitor, regulate, and evaluate landfill mitigation strategies [5].

286 This study is limited to only the largest emitting hotspots due to TROPOMI's  
287  $\sim 8 \text{ t h}^{-1}$  detection threshold [19]. The cumulative distribution of Climate TRACE  
288 emissions shows that 5% of global landfill methane emissions can be detected under  
289 this constraint (Supplementary Fig. S11b). While this study targets only 0.4% of  
290 landfills in the Climate TRACE dataset, these sites account for  $\sim 5\%$  of their estimated  
291 global landfill emissions ( $36.8 \text{ Tg yr}^{-1}$ ), a global total similar to the one from another  
292 independent inventory study ( $31.9 \text{ Tg yr}^{-1}$ ; 40). On the other hand, HSIs detect  
293 plumes only from the Tehran landfill among the Climate TRACE landfills emitting  
294 more than  $8 \text{ t h}^{-1}$ , suggesting large facility-level differences.

295 While the empirical detection limits are  $810 \text{ kg h}^{-1}$  for EnMAP and  $970 \text{ kg h}^{-1}$  for  
296 EMIT (Supplementary Section 5), this study's lowest two observed emission rates are  
297  $900$  and  $1,050 \text{ kg h}^{-1}$ , respectively. Considering the uncertainty of diffuse landfill emis-  
298 sions, we assume a detection threshold of  $1 \text{ t h}^{-1}$  for HSIs, up to 60% of solid waste  
299 emissions could be observable with global monitoring (Supplementary Fig. S11b).  
300 Thus, expanding HSI monitoring to more sites by increasing landfill target coverage  
301 and implementing automated plume detection [42, 43] will enable more comprehen-  
302 sive top-down information. Moreover, additional facility-level data will soon become  
303 available from satellites designed to observe methane and carbon dioxide, including  
304 MethaneSAT ( $100 \times 400 \text{ m}^2$  resolution) [44] and Carbon Mapper ( $\sim 35 \text{ m}$  resolution)  
305 [45]. To support all these, further validation with controlled releases from landfill-like  
306 sources is needed, particularly over complex terrain. As the suite of methane-observing  
307 satellites grows, we can improve our understanding of landfill emission distributions  
308 and variability, while supporting efforts to mitigate these emissions.



## 309 **Methods**

### 310 **Hyperspectral Imagers**

311 We combined three push-broom hyperspectral imagers (400–2500 nm) to detect global  
312 landfill methane emissions: EMIT [33, 34], launched on 14 July 2022 and operating on  
313 the International Space Station (ISS); EnMAP [46, 47], launched on 1 April 2022; and  
314 PRISMA [29, 30], launched on 22 March 2019. EnMAP and PRISMA provide 30 m  
315 spatial resolution over  $30 \times 30 \text{ km}^2$  scenes, while EMIT operates at 60 m resolution but  
316 covers a wider 80 km scene. EnMAP and PRISMA are in Sun-Synchronous Low Earth  
317 Orbits with equator crossing times of 11:00 and 10:30, respectively, while EMIT has a  
318 variable overpass time. At the strong methane absorption window ( $\sim 2300 \text{ nm}$ ), EMIT  
319 outperforms EnMAP and PRISMA with a SNR of  $\sim 500$  and a spectral resolution of  
320  $7.4 \text{ nm}$  [48]. In contrast, EnMAP’s SNR is twice that of PRISMA ( $\sim 180$ ), and its  
321 spectral resolution is  $2.7 \text{ nm}$  finer than PRISMA’s  $10 \text{ nm}$  resolution [27, 49].

322 Given the substantial size of the hyperspectral datasets, we initially focus on urban  
323 hot spots detected by TROPOMI (<https://methanedata.unep.org/>) where the wind  
324 rotation technique is used to determine the source location within a few km [14, 19].  
325 Then, we restrict our investigation to the surrounding area to determine whether the  
326 detected emissions originate from waste disposal sites or other sources and estimate  
327 their emission rates. Additionally, we analyze observations of the top 20 most emitting  
328 landfills from the Climate TRACE dataset.

### 329 **Methane Enhancement Retrieval**

330 We employ a linearized matched filter technique to retrieve methane enhancements  
331 ( $\Delta X\text{CH}_4$ ) in parts-per-billion (ppb) from the satellite observations. This approach has  
332 been successfully applied before to satellite and aircraft observations [26, 50–54]. The  
333 matched filter assumes a spectrally flat background and models the background radi-  
334 ance spectrum as a Gaussian distribution ( $\mathcal{N}$ ) with a mean vector  $\boldsymbol{\mu}$  and a covariance

335 matrix  $\Sigma$ . The radiance spectrum ( $L$ ) can be represented by two hypotheses:  $H_0$  for  
 336 radiance without a methane plume, and  $H_1$  with a plume present [50].

$$H_0 : L \sim \mathcal{N}(\boldsymbol{\mu}, \Sigma); H_1 : L \sim \mathcal{N}(\boldsymbol{\mu} + \Delta\text{XCH}_4 \mathbf{t}, \Sigma) \quad (1)$$

337 Here,  $\mathbf{t}$  represents the target signature, the product of the background mean radi-  
 338 ance ( $\boldsymbol{\mu}$ ) and the negative methane absorption coefficient ( $\mathbf{k}$ ). To determine  $\mathbf{k}$ , we  
 339 employ a forward model [55] and convolve the radiance with the imager’s central wave-  
 340 length and FWHM [50]. The atmosphere is divided into vertical layers with a thickness  
 341 of 1 km up to an altitude of 25 km, 2.5 km between 25 and 50 km, and 5 km above  
 342 50 km altitude. For the forward model simulation, methane enhancements are intro-  
 343 duced into the lowest layer at various values, ranging from 0 to 6400 ppb in double  
 344 increments of 100. The  $k$  value ( $\text{ppb}^{-1}$ ) for each band is calculated as the regression  
 345 slope between the natural logarithm of the radiance and the methane enhancements.  
 346 The maximum likelihood estimate of the scale factor  $\Delta\text{XCH}_4$  is:

$$\Delta\text{XCH}_4 = \frac{(\mathbf{t} - \boldsymbol{\mu})^T \Sigma^{-1} (\mathbf{L} - \boldsymbol{\mu})}{(\mathbf{t} - \boldsymbol{\mu})^T \Sigma^{-1} (\mathbf{t} - \boldsymbol{\mu})} \quad (2)$$

347 The strong absorption window (2100~2450 nm) is selected for the  $\Delta\text{XCH}_4$  cal-  
 348 culation. However, the results are often noisy in urban areas (due to complicated  
 349 reflectance related to for example roads and roofs), making it challenging to differen-  
 350 tiate plumes from the background. To mitigate this, we perform the same retrieval  
 351 over the 1300~2500 nm window [54], including both the strong ( $\sim 2300$  nm) and weak  
 352 ( $\sim 1700$  nm) methane absorption windows. Then, we apply a Chambolle total vari-  
 353 ance denoising (TV) filter [56] to obtain a smoothed  $\Delta\text{XCH}_4$  field. The TV filter aims

354 to minimize the cost function between the original and smoothed images. We gen-  
355 erate 300 plume-free noisy  $\Delta XCH_4$  images and determine the inflection point of the  
356 threshold versus denoising weight to exclude all falsely detected plumes [57]. Consid-  
357 ering the lower SNR of PRISMA, we select a denoising weight of 150, higher than the  
358 weight of 50 used for EMIT and EnMAP. The two-step denoised  $\Delta XCH_4$  field is only  
359 used for generating plume masks (Supplementary Section 3), while the emission rate  
360 calculation employs the  $\Delta XCH_4$  data without denoising.

### 361 **Emission Rate Quantification**

362 Supplementary Section 3 describes the process for generating a plume mask using the  
363 watershedding technique (Supplementary Fig. S4) [58, 59]. To account for the possibil-  
364 ity of strong and long plumes breaking the sparsity assumption of the matched filter,  
365 we exclude the plume pixels in each column of observations. Subsequently, we rerun  
366 the retrieval process to obtain the final emission rate products. This two-step approach  
367 helps mitigate the impact of dense plumes on the background radiance estimation and  
368 typically yields higher methane emission rates.

369 We then apply the IME method assuming concentrated sources [60, 61] to quantify  
370 the methane emission rates ( $Q$  in  $\text{kg h}^{-1}$ ):

$$Q = \frac{U_{\text{eff}} \cdot \text{IME}}{L} \quad (3)$$

371 where IME is the total methane mass (kg) in the plume mask,  $L$  (m) is the  
372 square root of the plume area, and  $U_{\text{eff}}$  is the effective wind speed (m/s). We perform  
373 instrument-specific calibrations for  $U_{\text{eff}}$  based on large-eddy simulations that model  
374 emissions from the landfill as an area source (Supplementary Section 3),  $U_{\text{eff}}$  depends  
375 linearly on the 10-m wind speed ( $U_{10}$ ):

$$\text{EMIT} : U_{\text{eff}} = 0.45 \cdot U_{10} + 0.67 \quad (4)$$

$$\text{EnMAP} : U_{\text{eff}} = 0.37 \cdot U_{10} + 0.69 \quad (5)$$

$$\text{PRISMA} : U_{\text{eff}} = 0.37 \cdot U_{10} + 0.70 \quad (6)$$

376 Our primary choice for the wind is the European Centre for Medium-Range  
377 Weather Forecasts Reanalysis 5 (ERA5) 10-m wind speed. However, we use the GEOS  
378 Forward Processing (GEOS-FP) data in cases where the ERA5 wind direction differs  
379 from the plume direction by more than 90 degrees. If both the ERA5 and GEOS-FP  
380 wind data fail to accurately capture the wind direction, we default to using the ERA5  
381 wind data.

### 382 **Climate TRACE Bottom-Up Inventory**

383 Climate TRACE is a global greenhouse gas emissions database [62]. The waste sector  
384 component uses Bayesian regression modeling that integrates detailed facility-level  
385 waste data from sources such as the US Environmental Protection Agency (EPA)  
386 [63], Waste Atlas (<http://www.atlas.d-waste.com/>), and Global Plastic Watch (GPW;  
387 <https://www.globalplasticwatch.org/>), to estimate methane emissions from solid waste  
388 disposal sites globally. The EPA data comes from 2021, while the Waste Atlas data  
389 corresponds to 2013, and the GPW data is from 2021. Country-level emissions are  
390 generally based on EDGAR estimates, except when the sum of facility-level emissions  
391 surpasses the EDGAR-reported figure.

### 392 **WasteMAP Platform**

393 WasteMAP (<https://wastemap.earth/>) is an online platform that compiles waste  
394 methane emission reports, model results, and observations. We only use the city-level

395 data estimated with the bottom-up Solid Waste Emissions Estimation Tool (SWEET)  
396 developed by the EPA. SWEET employs environmental factors and waste information  
397 from the World Bank What a Waste 2.0 report [3] to estimate methane emissions.

## 398 Data availability

399 The Level 1B data products for EMIT (version 1), EnMAP (version 1.4), and  
400 PRISMA (version 1) are available at the following links: [https://search.earthdata.](https://search.earthdata.nasa.gov/search?q=C2408009906-LPCLOUD)  
401 [nasa.gov/search?q=C2408009906-LPCLOUD](https://search.earthdata.nasa.gov/search?q=C2408009906-LPCLOUD), [https://www.enmap.org/data\\_access/](https://www.enmap.org/data_access/),  
402 and <https://prisma.asi.it/>. Retrieval and emission data will be available on Zenodo  
403 (<https://doi.org/10.5281/zenodo.13643544>). Notebooks to reproduce this work will  
404 be deposited on GitHub. HyperGas, the retrieval package, will become open-access  
405 following its publication.

## 406 References

- 407 [1] Intergovernmental Panel on Climate Change (IPCC). *Climate Change 2021 – The*  
408 *Physical Science Basis: Working Group I Contribution to the Sixth Assessment*  
409 *Report of the Intergovernmental Panel on Climate Change* (Cambridge University  
410 Press, Cambridge, 2023).
- 411 [2] Saunio, M. *et al.* The Global Methane Budget 2000–2017. *Earth Syst. Sci. Data*  
412 **12**, 1561–1623 (2020).
- 413 [3] Kaza, S., Yao, L. C., Bhada-Tata, P. & Van Woerden, F. *What a Waste 2.0*  
414 (Washington, DC: World Bank, 2018).
- 415 [4] COP29 Declaration on Reducing Methane from Organic Waste.  
416 [https://cop29.az/en/pages/cop29-declaration-on-reducing-methane-from-](https://cop29.az/en/pages/cop29-declaration-on-reducing-methane-from-organic-waste)  
417 [organic-waste](https://cop29.az/en/pages/cop29-declaration-on-reducing-methane-from-organic-waste).

- 418 [5] Bureau of Oceans and International Environmental and Scientific  
419 Affairs. Lowering Organic Waste Methane Initiative (LOW-Methane).  
420 <https://www.state.gov/lowering-organic-waste-methane-initiative-low-methane/>  
421 (2023).
- 422 [6] Duren, R. M. *et al.* California’s methane super-emitters. *Nature* **575**, 180–184  
423 (2019).
- 424 [7] Solazzo, E. *et al.* Uncertainties in the Emissions Database for Global Atmospheric  
425 Research (EDGAR) emission inventory of greenhouse gases. *Atmos. Chem. Phys.*  
426 **21**, 5655–5683 (2021).
- 427 [8] Cusworth, D. H. *et al.* Quantifying methane emissions from United States  
428 landfills. *Sci. Adv.* **383**, 1499–1504 (2024).
- 429 [9] Wang, Y. *et al.* Methane emissions from landfills differentially underestimated  
430 worldwide. *Nat. Sustain* **7**, 496–507 (2024).
- 431 [10] Miller, S. M. *et al.* Anthropogenic emissions of methane in the United States.  
432 *Proc. Natl. Acad. Sci.* **110**, 20018–20022 (2013).
- 433 [11] Singh, C. K., Kumar, A. & Roy, S. S. Quantitative analysis of the methane gas  
434 emissions from municipal solid waste in India. *Sci. Rep.* **8**, 2913 (2018).
- 435 [12] Cusworth, D. H. *et al.* Using remote sensing to detect, validate, and quantify  
436 methane emissions from California solid waste operations. *Environ. Res. Lett.*  
437 **15**, 054012 (2020).
- 438 [13] Spokas, K., Bogner, J. & Corcoran, M. Modeling landfill CH<sub>4</sub> emissions: CALMIM  
439 international field validation, using CALMIM to simulate management strategies,  
440 current and future climate scenarios. *Elem. Sci. Anth.* **9**, 00050 (2021).

- 441 [14] Maasackers, J. D. *et al.* Using satellites to uncover large methane emissions from  
442 landfills. *Sci. Adv.* **8**, eabn9683 (2022).
- 443 [15] Veefkind, J. P. *et al.* TROPOMI on the ESA Sentinel-5 Precursor: A GMES  
444 mission for global observations of the atmospheric composition for climate, air  
445 quality and ozone layer applications. *Remote Sens. Environ.* **120**, 70–83 (2012).
- 446 [16] Lorente, A. *et al.* Methane retrieved from TROPOMI: Improvement of the data  
447 product and validation of the first 2 years of measurements. *Atmos. Meas. Tech.*  
448 **14**, 665–684 (2021).
- 449 [17] Zhang, Y. *et al.* Quantifying methane emissions from the largest oil-producing  
450 basin in the United States from space. *Sci. Adv.* **6**, eaaz5120 (2020).
- 451 [18] Shen, L. *et al.* National quantifications of methane emissions from fuel exploita-  
452 tion using high resolution inversions of satellite observations. *Nat. Commun.* **14**,  
453 4948 (2023).
- 454 [19] Schuit, B. J. *et al.* Automated detection and monitoring of methane super-  
455 emitters using satellite data. *Atmos. Chem. Phys.* **23**, 9071–9098 (2023).
- 456 [20] Varon, D. J. *et al.* Satellite Discovery of Anomalously Large Methane Point  
457 Sources From Oil/Gas Production. *Geophys. Res. Lett.* **46**, 13507–13516 (2019).
- 458 [21] Dogniaux, M. *et al.* Satellite survey sheds new light on global solid waste methane  
459 emissions. *Preprint at <https://doi.org/10.31223/X5TB09>* (2024).
- 460 [22] Varon, D. J. *et al.* High-frequency monitoring of anomalous methane point sources  
461 with multispectral Sentinel-2 satellite observations. *Atmos. Meas. Tech.* **14**, 2771–  
462 2785 (2021).

- 463 [23] Pandey, S. *et al.* Daily detection and quantification of methane leaks using  
464 Sentinel-3: A tiered satellite observation approach with Sentinel-2 and Sentinel-  
465 5p. *Remote Sens. Environ.* **296**, 113716 (2023).
- 466 [24] Watine-Guiu, M., Varon, D. J., Irakulis-Loitxate, I., Balasus, N. & Jacob, D. J.  
467 Geostationary satellite observations of extreme and transient methane emissions  
468 from oil and gas infrastructure. *Proc. Natl. Acad. Sci.* **120**, e2310797120 (2023).
- 469 [25] Guanter, L. *et al.* Mapping methane point emissions with the PRISMA  
470 spaceborne imaging spectrometer. *Remote Sens. Environ.* **265**, 112671 (2021).
- 471 [26] Thorpe, A. K. *et al.* Attribution of individual methane and carbon dioxide  
472 emission sources using EMIT observations from space. *Sci. Adv.* **9**, eadh2391  
473 (2023).
- 474 [27] Roger, J. *et al.* High-resolution methane mapping with the EnMAP satellite  
475 imaging spectroscopy mission. *IEEE Trans. Geosci. Remote Sens.* **62**, 1–12  
476 (2024).
- 477 [28] Thorpe, A. K. *et al.* Improved methane emission estimates using AVIRIS-NG and  
478 an Airborne Doppler Wind Lidar. *Remote Sens. Environ.* **266**, 112681 (2021).
- 479 [29] Loizzo, R. *et al.* Prisma: The Italian Hyperspectral Mission (2018).
- 480 [30] Cogliati, S. *et al.* The PRISMA imaging spectroscopy mission: Overview and first  
481 performance analysis. *Remote Sens. Environ.* **262**, 112499 (2021).
- 482 [31] Sherwin, E. D. *et al.* Single-blind validation of space-based point-source detection  
483 and quantification of onshore methane emissions. *Sci. Rep.* **13**, 3836 (2023).
- 484 [32] Sherwin, E. D. *et al.* Single-blind test of nine methane-sensing satellite systems  
485 from three continents. *Atmos. Meas. Tech.* **17**, 765–782 (2024).



- 486 [33] Green, R. O. *et al.* The Earth Surface Mineral Dust Source Investigation: An  
487 Earth Science Imaging Spectroscopy Mission (2020).
- 488 [34] Green, R. O. *et al.* Performance and Early Results from the Earth Surface Mineral  
489 Dust Source Investigation (EMIT) Imaging Spectroscopy Mission (2023).
- 490 [35] Esri, Maxar, Geographics, E. & the GIS User Community. ESRI World Imagery.  
491 [https://services.arcgisonline.com/ArcGIS/rest/services/World\\_Imagery/MapServer](https://services.arcgisonline.com/ArcGIS/rest/services/World_Imagery/MapServer)  
492 (2022).
- 493 [36] Toha, M. & Rahman, M. M. Estimation and prediction of methane gas generation  
494 from landfill sites in Dhaka city, Bangladesh. *Case Stud. Chem. Environ. Eng.* **7**,  
495 100302 (2023).
- 496 [37] Carbon Mapper data. Retrieved from <https://data.carbonmapper.org> (2024).
- 497 [38] Sentinel-2 Cloud-Optimized GeoTIFFs. [https://registry.opendata.aws/sentinel-](https://registry.opendata.aws/sentinel-2-12a-cogs/)  
498 [2-12a-cogs/](https://registry.opendata.aws/sentinel-2-12a-cogs/) (2024).
- 499 [39] Karion, A. *et al.* Methane Emissions Show Recent Decline but Strong Seasonality  
500 in Two US Northeastern Cities. *Environ. Sci. Technol.* **57**, 19565–19574 (2023).
- 501 [40] Höglund-Isaksson, L., Gómez-Sanabria, A., Klimont, Z., Rafaj, P. & Schöpp,  
502 W. Technical potentials and costs for reducing global anthropogenic methane  
503 emissions in the 2050 timeframe –results from the GAINS model. *Environ. Res.*  
504 *Commun.* **2**, 025004 (2020).
- 505 [41] Ocko, I. B. *et al.* Acting rapidly to deploy readily available methane mitigation  
506 measures by sector can immediately slow global warming. *Environ. Res. Lett.* **16**,  
507 054042 (2021).

- 508 [42] Růžička, V. *et al.* Semantic segmentation of methane plumes with hyperspectral  
509 machine learning models. *Sci. Rep.* **13**, 19999 (2023).
- 510 [43] Kumar, S., Arevalo, I., Iftekhar, ASM. & Manjunath, BS. Methanemap-  
511 per: Spectral absorption aware hyperspectral transformer for methane detection  
512 (2023).
- 513 [44] Rohrschneider, R. *et al.* The MethaneSAT Mission. *Small Satellite Conference*  
514 (2021).
- 515 [45] Keremedjiev, M. *et al.* Carbon mapper phase 1: Two upcoming VNIR-SWIR  
516 hyperspectral imaging satellites (2022).
- 517 [46] Guanter, L. *et al.* The EnMAP Spaceborne Imaging Spectroscopy Mission for  
518 Earth Observation. *Remote Sens.* **7**, 8830–8857 (2015).
- 519 [47] Storch, T. *et al.* The EnMAP imaging spectroscopy mission towards operations.  
520 *Remote Sens. Environ.* **294**, 113632 (2023).
- 521 [48] Thompson, D. R. *et al.* On-orbit calibration and performance of the EMIT  
522 imaging spectrometer. *Remote Sens. Environ.* **303**, 113986 (2024).
- 523 [49] Cusworth, D. H. *et al.* Potential of next-generation imaging spectrometers to  
524 detect and quantify methane point sources from space. *Atmos. Meas. Tech.* **12**,  
525 5655–5668 (2019).
- 526 [50] Thompson, D. R. *et al.* Real-time remote detection and measurement for airborne  
527 imaging spectroscopy: A case study with methane. *Atmos. Meas. Tech.* **8**, 4383–  
528 4397 (2015).
- 529 [51] Thompson, D. R. *et al.* Space-based remote imaging spectroscopy of the Aliso  
530 Canyon CH<sub>4</sub> superemitter. *Geophys. Res. Lett.* **43**, 6571–6578 (2016).

- 531 [52] Foote, M. D. *et al.* Fast and Accurate Retrieval of Methane Concentration From  
532 Imaging Spectrometer Data Using Sparsity Prior. *IEEE Trans. Geosci. Remote*  
533 *Sens.* **58**, 6480–6492 (2020).
- 534 [53] Foote, M. D. *et al.* Impact of scene-specific enhancement spectra on matched  
535 filter greenhouse gas retrievals from imaging spectroscopy. *Remote Sens. Environ.*  
536 **264**, 112574 (2021).
- 537 [54] Roger, J., Guanter, L., Gorroño, J. & Irakulis-Loitxate, I. Exploiting the entire  
538 near-infrared spectral range to improve the detection of methane plumes with  
539 high-resolution imaging spectrometers. *Atmos. Meas. Tech.* **17**, 1333–1346 (2024).
- 540 [55] Gloudemans, A. M. S., Schrijver, H., Hasekamp, O. P. & Aben, I. Error analysis  
541 for CO and CH<sub>4</sub> total column retrievals from SCIAMACHY 2.3  $\mu$ m spectra.  
542 *Atmos. Chem. Phys.* **8**, 3999–4017 (2008).
- 543 [56] Chambolle, A. An Algorithm for Total Variation Minimization and Applications.  
544 *J. Math. Imaging Vis.* **20**, 89–97 (2004).
- 545 [57] Chan Miller, C. *et al.* Methane retrieval from MethaneAIR using the CO<sub>2</sub> proxy  
546 approach: A demonstration for the upcoming MethaneSAT mission. *Atmos. Meas.*  
547 *Tech.* **17**, 5429–5454 (2024).
- 548 [58] Heikenfeld, M. *et al.* Tobac 1.2: Towards a flexible framework for tracking and  
549 analysis of clouds in diverse datasets. *Geosci. Model Dev.* **12**, 4551–4570 (2019).
- 550 [59] Zhang, X. *et al.* Spaceborne Observations of Lightning NO<sub>2</sub> in the Arctic.  
551 *Environ. Sci. Technol.* **57**, 2322–2332 (2023).
- 552 [60] Frankenberg, C. *et al.* Airborne methane remote measurements reveal heavy-tail  
553 flux distribution in Four Corners region. *Proc. Natl. Acad. Sci.* **113**, 9734–9739

554 (2016).

555 [61] Varon, D. J. *et al.* Quantifying methane point sources from fine-scale satellite  
556 observations of atmospheric methane plumes. *Atmos. Meas. Tech.* **11**, 5673–5686  
557 (2018).

558 [62] Climate TRACE - Tracking Real-time Atmospheric Carbon Emissions. Climate  
559 TRACE Emissions Inventory (2024).

560 [63] US EPA, OAR. Inventory of U.S. Greenhouse Gas Emissions and Sinks:  
561 1990-2021. [https://www.epa.gov/ghgemissions/inventory-us-greenhouse-gas-](https://www.epa.gov/ghgemissions/inventory-us-greenhouse-gas-emissions-and-sinks-1990-2021)  
562 [emissions-and-sinks-1990-2021](https://www.epa.gov/ghgemissions/inventory-us-greenhouse-gas-emissions-and-sinks-1990-2021) (2023).

1                   **Supporting Information for**  
2                   Global identification of solid waste methane super  
3                   emitters using hyperspectral satellites

4                   Xin Zhang<sup>1\*</sup>, Joannes D. Maasackers<sup>1</sup>, Javier Roger<sup>2</sup>,  
5                   Luis Guanter<sup>2,3</sup>, Shubham Sharma<sup>1</sup>, Srijana Lama<sup>1</sup>, Paul Tol<sup>1</sup>,  
6                   Daniel J. Varon<sup>4</sup>, Daniel H. Cusworth<sup>5</sup>, Katherine Howell<sup>5</sup>,  
7                   Andrew K. Thorpe<sup>6</sup>, Philip G. Brodrick<sup>6</sup>, Ilse Aben<sup>1,7</sup>

8                   <sup>1\*</sup>SRON Netherlands Institute for Space Research, Leiden, 2333 CA,  
9                   The Netherlands.

10                  <sup>2</sup>Research Institute of Water and Environmental Engineering,  
11                  Universitat Politècnica de València, Valencia, 46022, Spain.

12                  <sup>3</sup>Environmental Defense Fund, Amsterdam, 1083 HN, The Netherlands.

13                  <sup>4</sup>School of Engineering and Applied Sciences, Harvard University,  
14                  Cambridge, 02138, MA, USA.

15                  <sup>5</sup>Carbon Mapper, Pasadena, 91105, CA, USA.

16                  <sup>6</sup>Jet Propulsion Laboratory, California Institute of Technology,  
17                  Pasadena, 91109, CA, USA.

18                  <sup>7</sup>Department of Earth Sciences, Vrije Universiteit Amsterdam,  
19                  Amsterdam, 1081 HV, The Netherlands.

20                  \*Corresponding author(s). E-mail(s): [xin.zhang@sron.nl](mailto:xin.zhang@sron.nl);

## 21 Contents

22	<b>1 Emission uncertainty quantification</b>	<b>2</b>
23	<b>2 Comparison with controlled releases</b>	<b>3</b>
24	<b>3 IME calibration and plume mask</b>	<b>4</b>
25	<b>4 Comparison with Carbon Mapper EMIT quantifications</b>	<b>8</b>
26	<b>5 Detection limit</b>	<b>9</b>

## 27 1 Emission uncertainty quantification

28 There are three sources of uncertainty in our emission uncertainty estimations: wind  
29 speed error, retrieval random error, and uncertainty in the integrated mass enhance-  
30 ment (IME) calibration [1–3]. For the error in the wind speed, we compare the  
31 European Centre for Medium-Range Weather Forecasts Reanalysis 5 (ERA5) 10-m  
32 wind data with the automated Surface Observing System (ASOS) dataset obtained  
33 from worldwide airports (<https://mesonet.agron.iastate.edu/ASOS/>). We only include  
34 the wind data recorded between 10:00 and 14:00 (local time) to coincide with HSI  
35 overpass times. The standard deviation of the difference between ERA5 and ASOS  
36 wind data, is  $\sim 1.5 \text{ m s}^{-1}$  for wind speeds higher than 3 m/s. For wind speeds lower  
37 than 3 m/s, we apply a relative wind error of 50% [4]. We also compare the ERA5  
38 and GEOS Forward Processing (GEOS-FP) wind reanalysis data and find that their  
39 difference falls within our wind uncertainty estimate.

40 To quantify the effects of retrieval random error, we apply the plume mask to  
41 non-plume pixels across the entire scene and calculate the standard deviation of the  
42 emission rates [1]. The last component of uncertainty is the IME calibration (Section  
43 3) error. The area-source calibration that we use assumes a uniform distribution of  
44 methane emissions across a  $275 \times 275 \text{ m}^2$  area, whereas the real distribution can be

45 more complex [3]. To estimate the uncertainty originating from this simplification, we  
46 change the effective wind calibration to one that is calibrated using point sources and  
47 calculate the resulting change in emission rate [3].

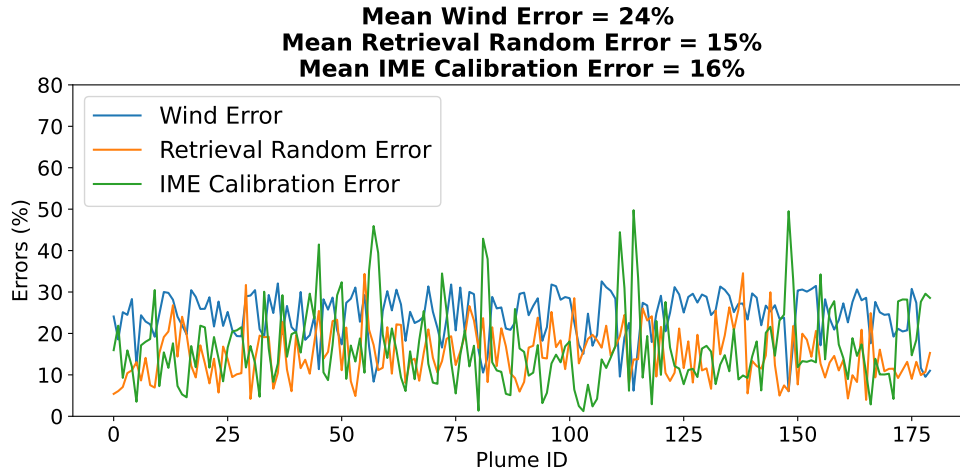


**Fig. S1** Relative estimation uncertainties from wind (blue), retrieval random error (orange), and IME calibration error (green). The wind error is set as  $1.5 \text{ m s}^{-1}$  for wind speeds higher than  $3 \text{ m/s}$ , while it is  $50\%$  for wind speeds lower than  $3 \text{ m/s}$ . The random error is estimated using the standard deviation of emission rates obtained by shifting the plume mask to non-plume pixels across the entire scene. The plume IDs on the x-axis are arranged chronologically.

48 Overall, the uncertainties associated with wind speed error, retrieval random error,  
49 and IME calibration error are  $24\%$ ,  $15\%$ , and  $16\%$ , respectively (Fig. S1). To estimate  
50 the uncertainty in individual estimates or summation of methane emissions from dif-  
51 ferent landfills, we calculate the square root of the sum of the squares of the individual  
52 uncertainties.

## 53 2 Comparison with controlled releases

54 We validate our emission quantification by comparing the derived emission rates with  
55 controlled methane releases conducted in 2021 and 2022 (Fig. S2). For the EnMAP  
56 controlled release, the actual release rate was  $1.1 \text{ t h}^{-1}$ , while our estimation yields

57  $1.6 \pm 0.5 \text{ t h}^{-1}$ , which agrees with the estimations from other analysis teams ranging  
58 from  $1.5$  to  $1.8 \text{ t h}^{-1}$  [5]. Similarly, for the PRISMA controlled release, our estimation  
59 is  $5.2 \pm 1.8 \text{ t h}^{-1}$ , while the actual release rate was  $4.5 \text{ t h}^{-1}$ , and other analysis teams  
60 estimated emission rates within the range of  $3.6$  to  $5.0 \text{ t h}^{-1}$  [6].

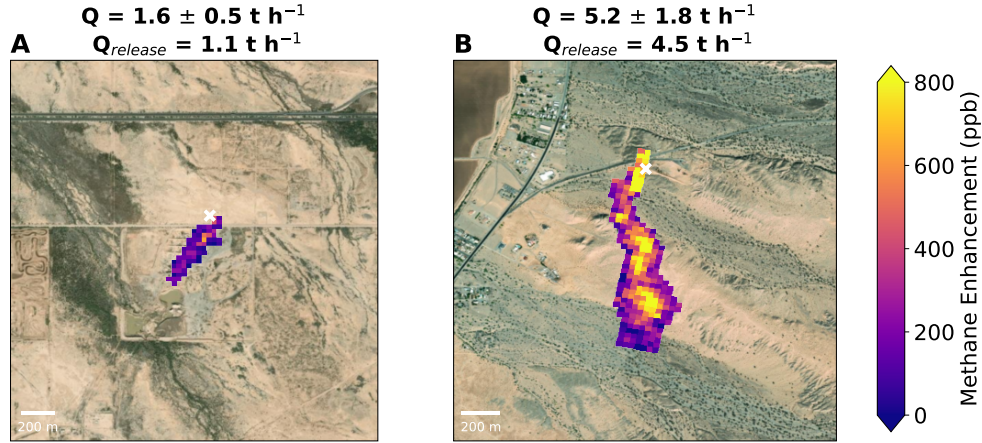


**Fig. S2** Methane enhancements observed by (A) EnMAP on November 16, 2022, and (B) PRISMA on October 21, 2021, for two controlled methane release experiments [5, 6]. Our estimates  $1.6 \pm 0.5 \text{ t h}^{-1}$  and  $5.2 \pm 1.8 \text{ t h}^{-1}$  compare well with the actual releases of  $1.1 \text{ t h}^{-1}$  and  $4.5 \text{ t h}^{-1}$  respectively. The release sites are marked with a white 'x'. Background imagery comes from Esri World Imagery [7].

### 61 3 IME calibration and plume mask

62 To calibrate the effective wind speed used in the IME calculation against reanalysis  
63 10 m wind speeds, we employ Weather and Research Model large-eddy simulations  
64 (WRF-LES) for two source types: a  $275 \times 275 \text{ m}^2$  area source (e.g., like a landfill  
65 [3]) and a point source (e.g., oil & gas and underground coal mining facilities). We  
66 randomly scale source rates from  $1$  to  $30 \text{ t h}^{-1}$  and add normally distributed measure-  
67 ment noise (Fig. S3A). Noise levels are defined by standard deviations of non-plume  
68 methane enhancement in clear-sky hyperspectral scenes, with precisions of 3%, 5%,  
69 and 12% for EMIT, EnMAP, and PRISMA, respectively. For each plume, the effective



70 wind speed ( $U_{\text{eff}}$ ) is computed from  $QL/\text{IME}$ , where the emission rate ( $Q$ ) is known,  
71 and plume length ( $L$ , square root of the plume area) and IME are calculated from  
72 plume masks.

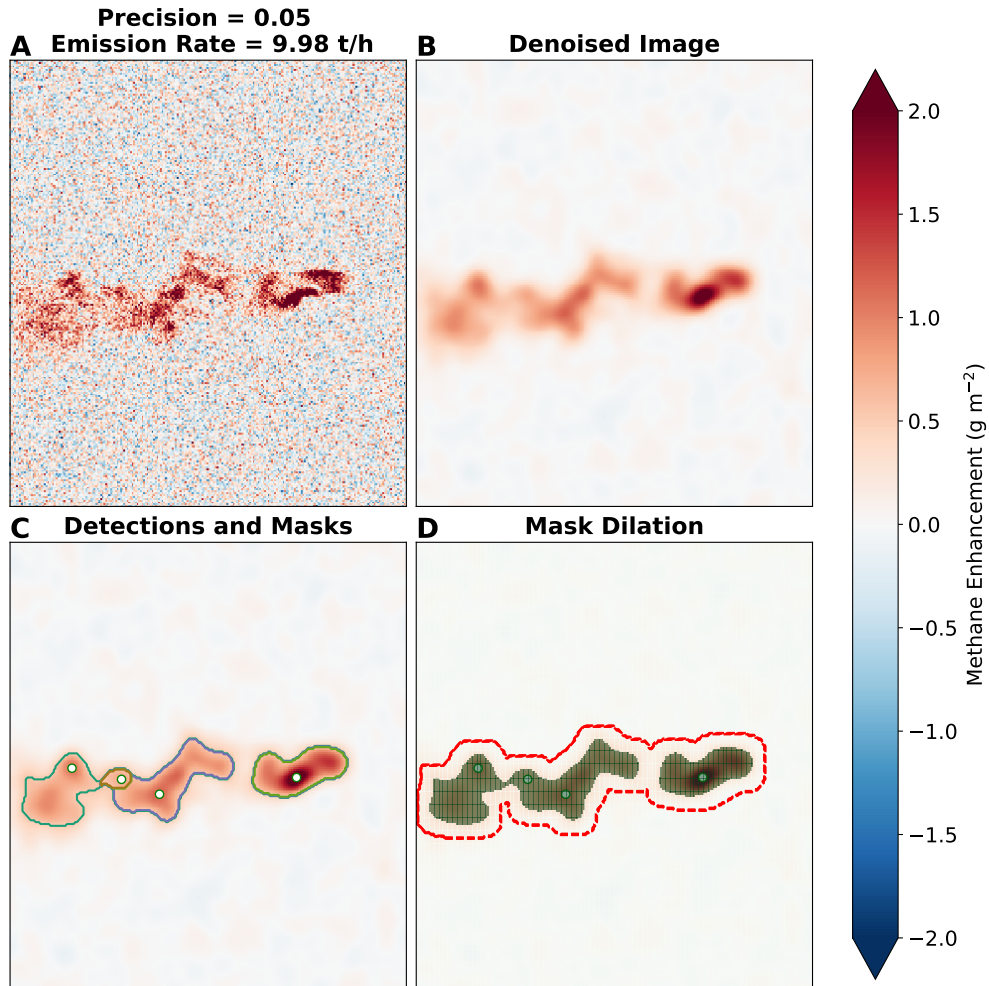


**Fig. S3** Plume mask generation process for methane emissions using WRF-LES simulation. (A) Methane enhancement ( $\Delta X_{\text{CH}_4}$ ) with added Gaussian noise ( $\sigma=0.05 \times 1875$  ppb). (B) Denoised  $\Delta X_{\text{CH}_4}$  field after applying a Chambolle total variation (TV) denoising filter. (C) Initial plume masks derived from the watershedding algorithm. White dots indicate high- $\Delta X_{\text{CH}_4}$  locations; contours represent individual masks. (D) Final plume mask (dark green): initial masks expanded by 180 m and combined (red).

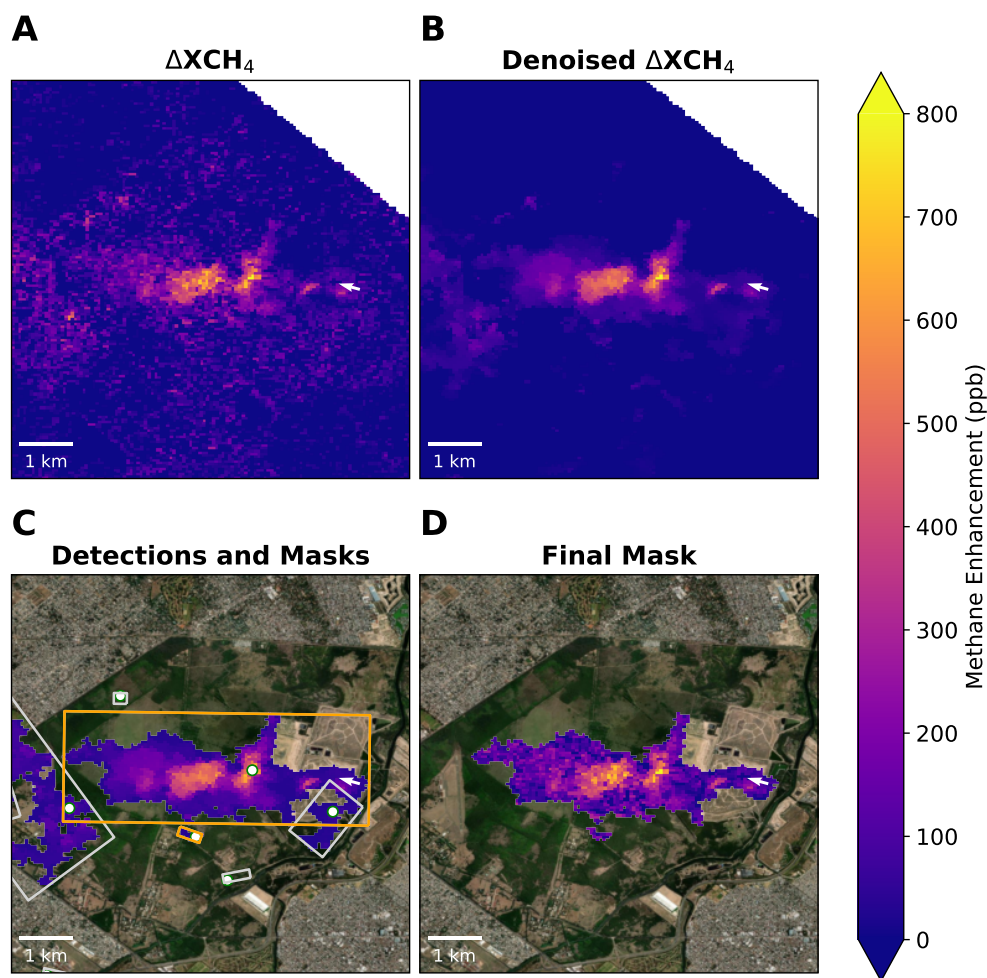


**Fig. S4** Plume mask creation process for the Norte III landfill methane emission using the EMIT observation on November 24, 2023. The white pixels represent missing data (outside the EMIT image swath), while the white arrow indicates the ERA5 wind direction. (A) Methane enhancement ( $\Delta XCH_4$ ) derived from the strong  $CH_4$  absorption window (2100~2450 nm). (B) Denoised  $\Delta XCH_4$  field obtained by applying the Chambolle total variance denoising (TV) filter to  $\Delta XCH_4$  within the 1300~2500 nm window. (C) Initial plume masks derived from watershedding algorithm. White dots indicate high- $\Delta XCH_4$  locations; rectangles represent the minimum rotated rectangles for each mask, with orange rectangles indicating azimuth differences less than  $30^\circ$ . (D) Final  $\Delta XCH_4$  plume mask.

73 We derive methane plume masks by applying a watershedding technique to  
 74 denoised methane fields (Fig. S3B). This method has been applied to track convective  
 75 clouds [8] and nitrogen dioxide plumes in TROPOMI observations [9]. It treats pixel  
 76 values as a topographic surface and separates them into catchment basins. Threshold

77 values of 2 and 3 standard deviations are used to identify multiple localized high-  
 78 enhancement features and nearby areas with high enhancement values (Fig. S3C). We  
 79 dilate these masks by 180 m and merge overlapping masks, with the mask containing  
 80 the emission source used to identify masks from a single source (Fig. S3D). Figure S4  
 81 demonstrates the plume mask determined for a Norte III landfill methane emission  
 82 plume. To ensure plumes originate from the same source, we limit the azimuth dif-  
 83 ference of the oriented envelope (minimum rotated rectangle) to less than  $30^\circ$  (Fig.  
 84 S4C), assuming minimal wind direction changes around the landfill. Non-detects are  
 85 classified if no plume mask covers the source of interest.

86 Figure S5 shows the relationship between  $U_{\text{eff}}$  and  $U_{10}$  inferred from the LES  
 87 ensemble. We use the area-source calibration by default and the point-source calibra-  
 88 tion to estimate calibration error.

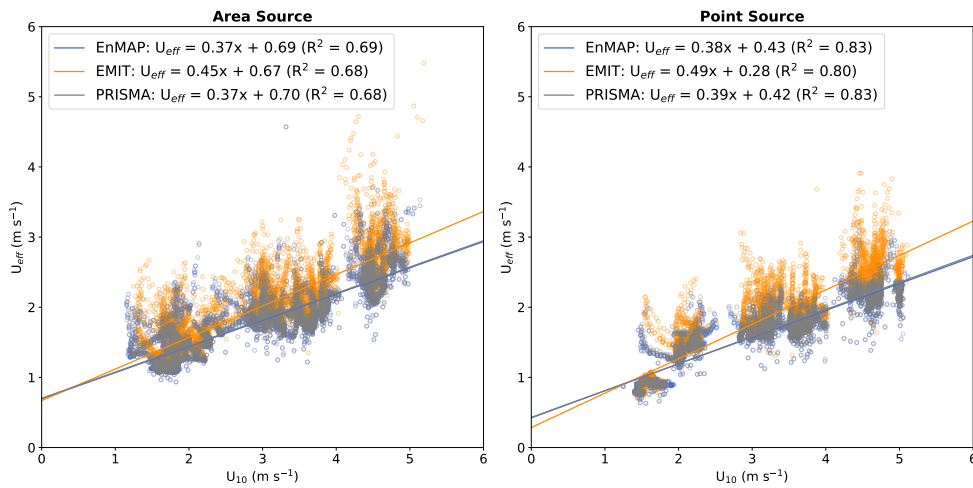


**Fig. S5** Relationship between the effective and local 10 m wind speeds for different instrument precisions and source types based on WRF LES simulations.

## 89 4 Comparison with Carbon Mapper EMIT 90 quantifications

91 Carbon Mapper (<https://data.carbonmapper.org>) provides methane emission rate  
92 estimates for EMIT using a method we call 'IME-fetch', which only uses the first 2500  
93 m of the plume to perform the quantification. We apply this method and compare the  
94 results to our IME results. The IME-fetch method consists of the following steps: 1)  
95 Center the Level 2B methane enhancement map on the plume origin, covering an area  
96 of  $\pm 2500$  m in both horizontal directions. 2) Use a 90th percentile threshold with a  
97 1000 m crop to distinguish between the background and plume enhancements. Iden-  
98 tify pixels exceeding this threshold and group them into connected clusters. Consider  
99 only clusters with at least 5 pixels as part of the plume. 3) Apply a proximity criterion  
100 to each cluster group, excluding separated clusters more than 15 pixels away from the  
101 plume origin. The emission rate is calculated as  $\text{IME-fetch} \cdot U_{10} / L$ , where  $U_{10}$  is the  
102 mean 10 m wind speed in the plume mask (the method does not rely on an effective  
103 wind speed) and  $L$  is the maximum distance from the plume origin to another point  
104 along the segmented plume's convex hull.

105 Figure S6A compares source rates retrieved from both IME and IME-fetch methods  
106 to the true source rates from WRF-LES. While the IME method shows good agreement  
107 (slope=0.99,  $R^2=0.93$ ) due to calibration, the IME-fetch results underestimate the  
108 emission rates (slope=0.77,  $R^2=0.89$ ). This disagreement is mainly due to differences in  
109 used plume length (Fig. S6B), which depends on the plume masking method. Our IME  
110 method (Section 3) uses a smoother plume mask without fetch distance limitations,  
111 leading to more plume pixels for longer plumes. This trend is also observed in real  
112 EMIT observations (Fig. S6C), but with greater magnitude. Further research is needed  
113 to accurately reproduce both trend and magnitude, which will help address potential  
114 biases in quantification.

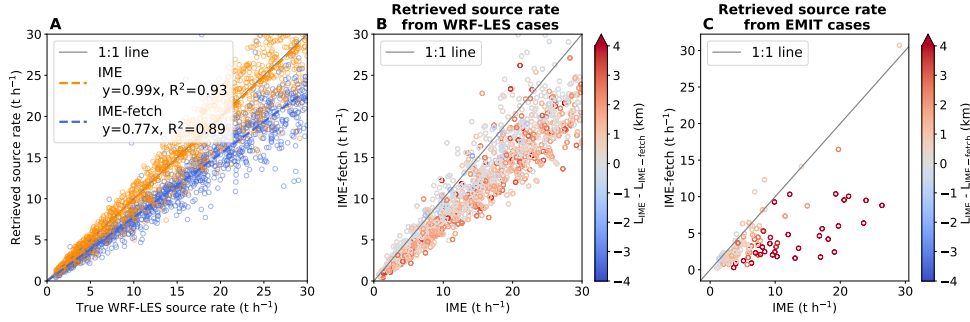


**Fig. S6** (A) Comparison of the IME (this study) and IME-fetch (Carbon Mapper) methods for estimating source rates using the WRF-LES test set for EMIT. (B) Correlation between IME and IME-fetch values as a function of plume length difference. (C) Same as (B), but from 127 EMIT observations over 36 landfills in this study.

## 115 5 Detection limit

116 The theoretical point-source methane detection limit ( $Q_{min}$ ) of instruments can be  
 117 derived from:

$$Q_{min} = PUGq \quad (1)$$

118 where  $P$  is the methane precision ( $\text{kg m}^{-2}$ , see Section 3),  $U$  is the mean wind  
 119 speed ( $3 \text{ m s}^{-2}$  used here),  $G$  is the ground sampling distance (m), and  $q$  is a constant  
 120 equal to 5 for quantification [10, 11]. This results in detection limits of  $810 \text{ kg h}^{-1}$  for  
 121 EnMAP and  $970 \text{ kg h}^{-1}$  for EMIT. For the EnMAP observations in this study, we  
 122 find one plume with an emission rate below  $1 \text{ t h}^{-1}$  and 8 plumes with emission rates  
 123 between 1 and  $2 \text{ t h}^{-1}$ . The EMIT data show 10 plumes with emission rates between  
 124 1 and  $2 \text{ t h}^{-1}$ , but none below  $1 \text{ t h}^{-1}$ .

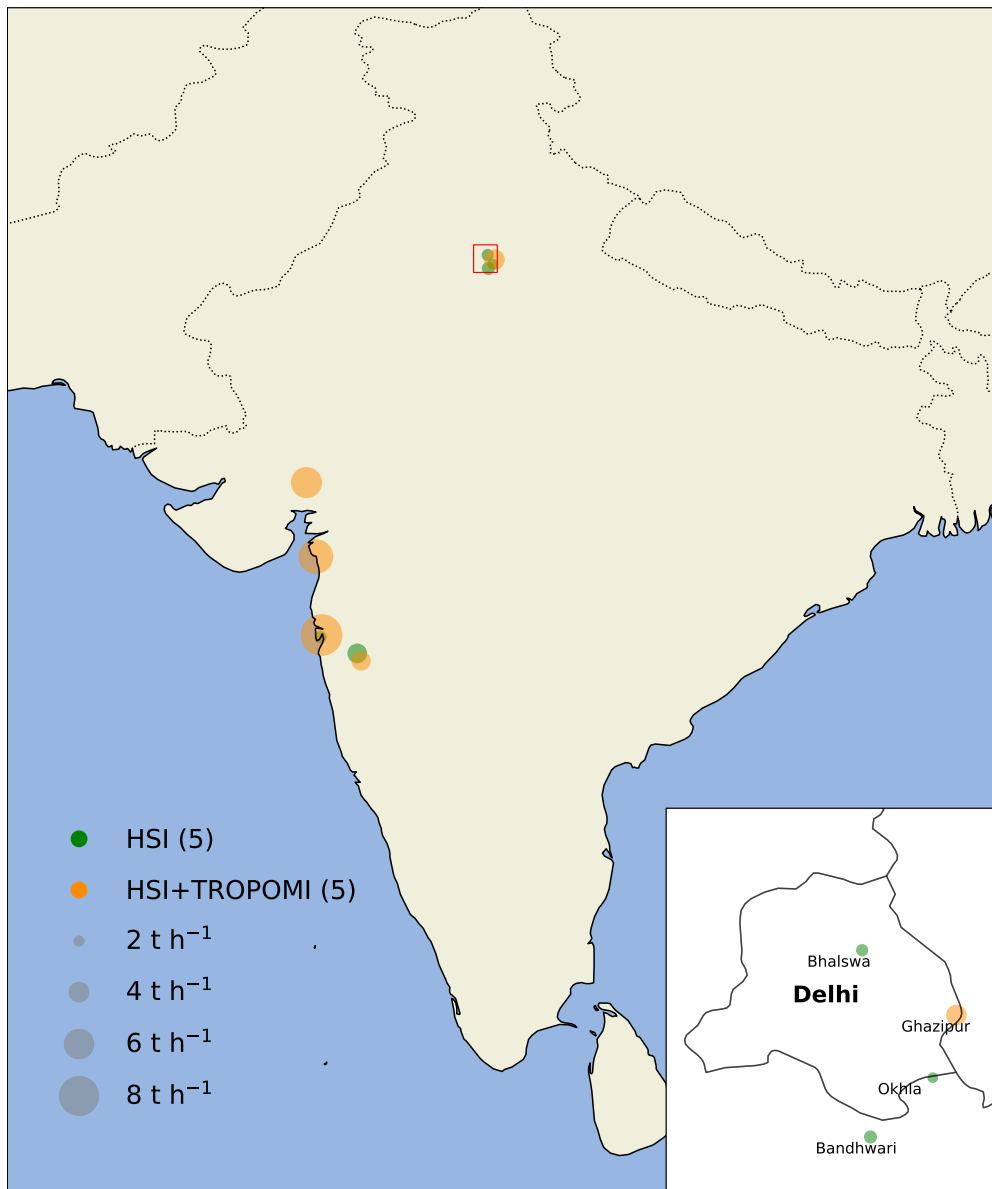


**Fig. S7** Landfill emissions detected by HSI across India, with a zoomed-in view of the Delhi region.

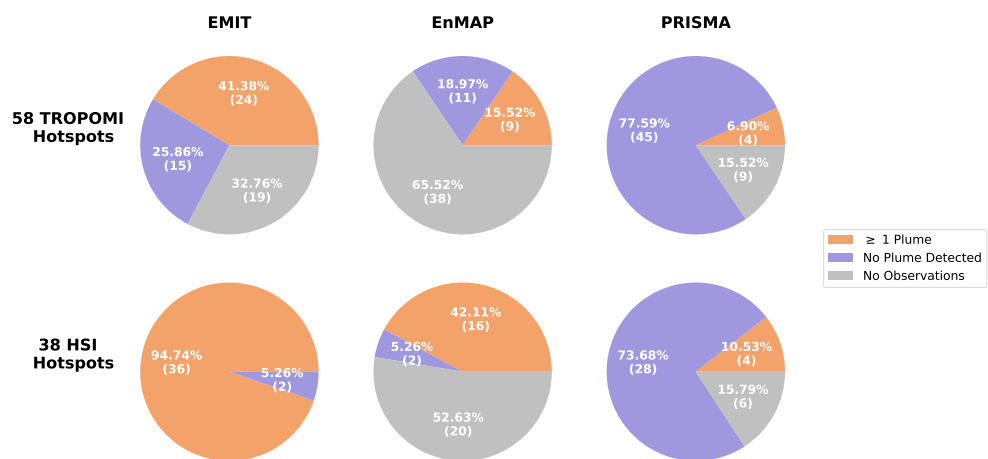


**Fig. S8** Variation in landfill hot spots detection efficiency by different HSIs (EMIT, EnMAP, and PRISMA) distinguishing three categories: detection of at least one plume (orange), clear-sky observations without detected plumes (purple), and no clear-sky observations (grey). Corresponding percentage values are displayed next to the number of hot spots in each category.

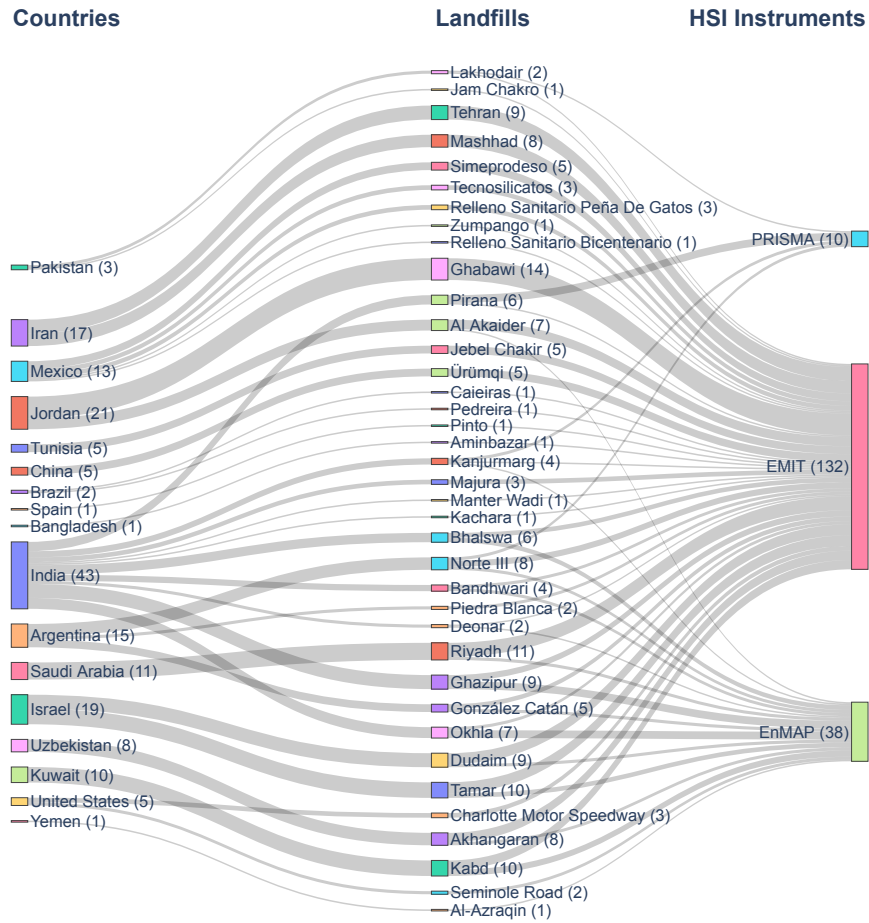


**Fig. S9** Sankey plot for the numbers of landfill plumes detected by HSIs (EMIT, EnMAP, and PRISMA). The numbers beside each country represent the total number of plumes detected from landfills within that country; the numbers next to each landfill indicate the number of detected plumes, and the numbers on the right show the total observations per HSI instrument.



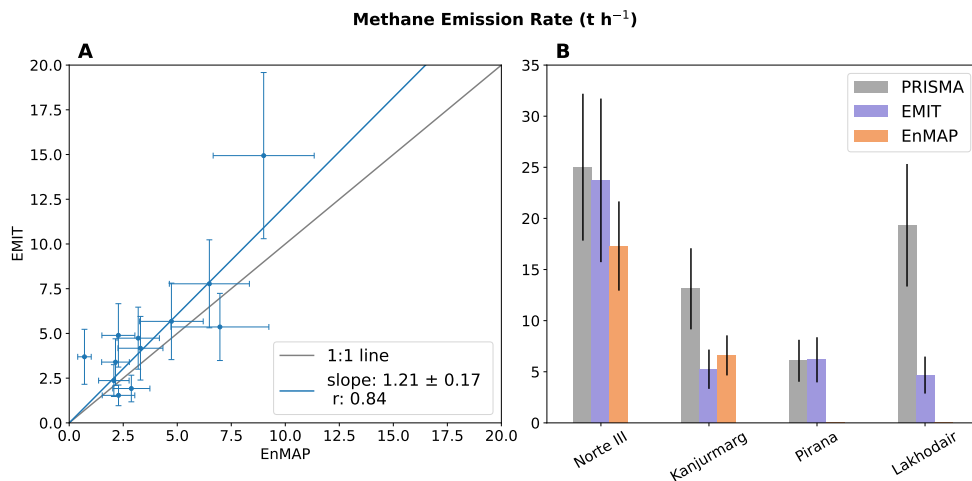


**Fig. S10** Comparison of average methane emission rates estimated with different HSIs for the same 24 landfill sites. (A) The orthogonal distance regression between methane emission rates estimated using the EMIT and EnMAP HSI sensors. (B) The methane emission rates of the four landfills with methane plumes detected by PRISMA. Observations were made by EMIT and EnMAP in 2023 for all sites. PRISMA observations were from 2023 for the Norte III and Pirana landfills, and 2020–2022 for the Kanjurmarg and Lakhodair landfills.

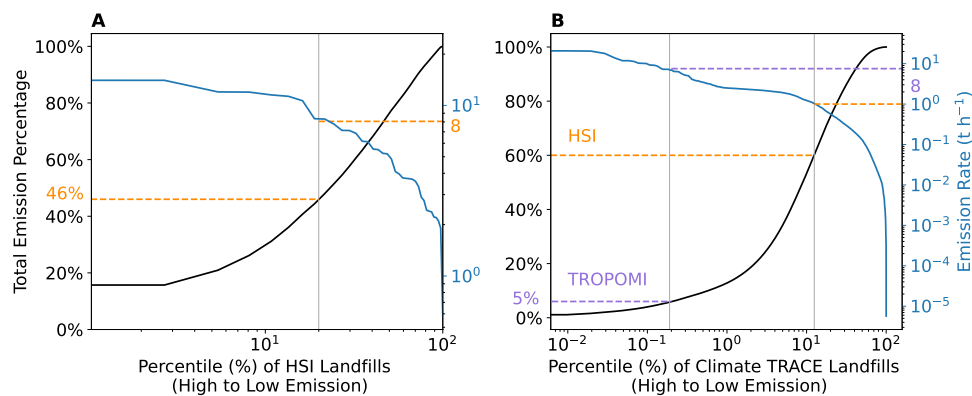


**Fig. S11** Cumulative distributions of landfill methane emissions. The black lines represent the cumulative distribution function of summed emission rates across landfill percentiles (in descending order), while the blue line indicates the emission rates at each respective percentile. (A) Landfills identified by HSIs. The top 20% of the highest emitting landfills emit 46% of total HIS-detected landfill emissions. (B) Landfills in the Climate TRACE dataset. The  $1 t h^{-1}$  limit (orange line) and the  $8 t h^{-1}$  limit (purple line) correspond to the estimated detection thresholds of HSI and TROPOMI, respectively.

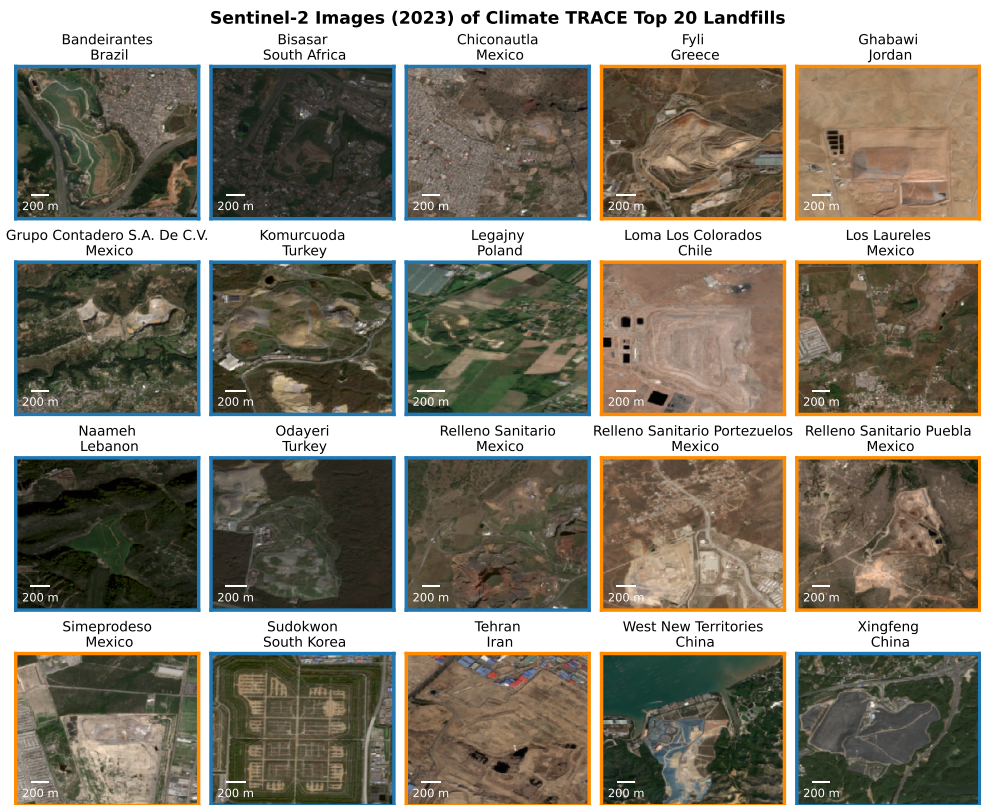


**Fig. S12** Sentinel-2 satellite images from 2023 [12] showing the top 20 emitting landfills identified in the Climate TRACE dataset. An orange frame indicates that the HSIs detected methane plumes, while a blue frame means they did not.

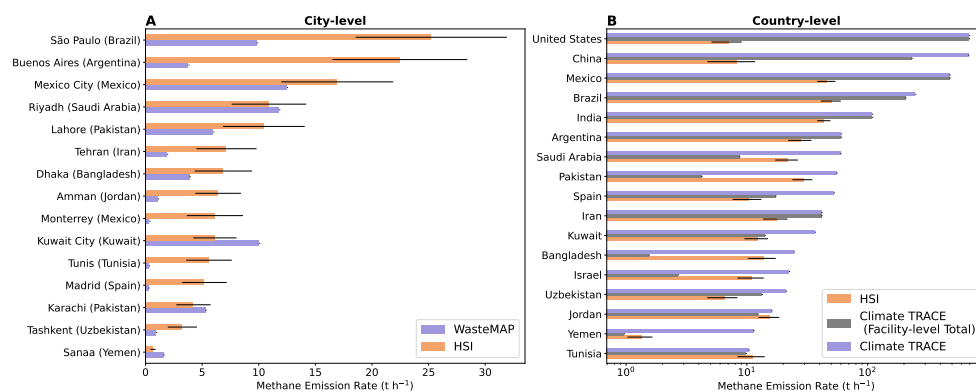


**Fig. S13** Comparison of methane emissions from landfills summed at the (A) city and (B) country levels, estimated using HSI observations, WasteMAP, and Climate TRACE inventories. The emission rates calculated using HSI represent the total emissions from measured and analyzed landfills in each city and country (Table S6 and S7). The total facility emissions for each country (not just the landfills analyzed using the HSI), as reported by Climate TRACE, are shown in gray.

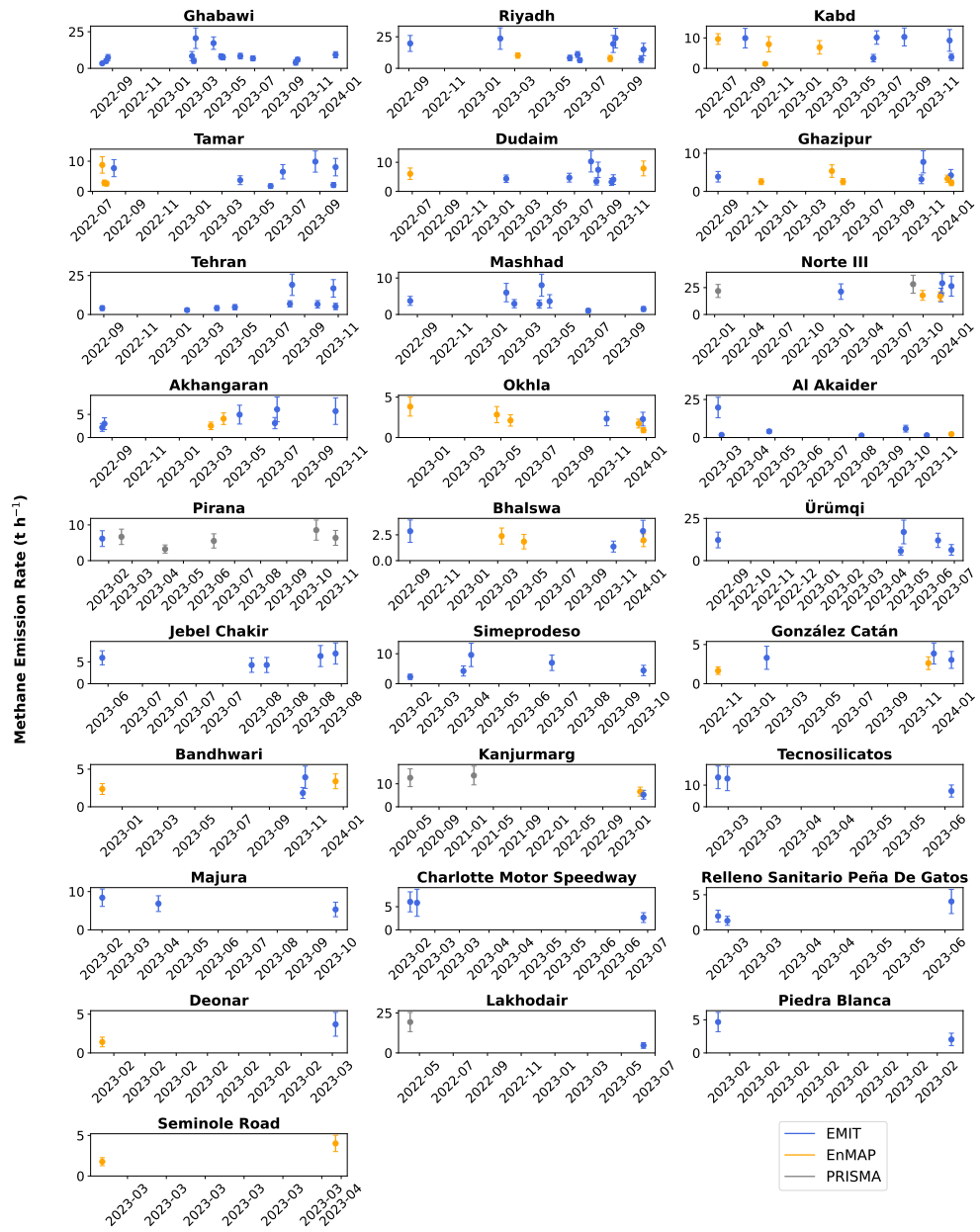
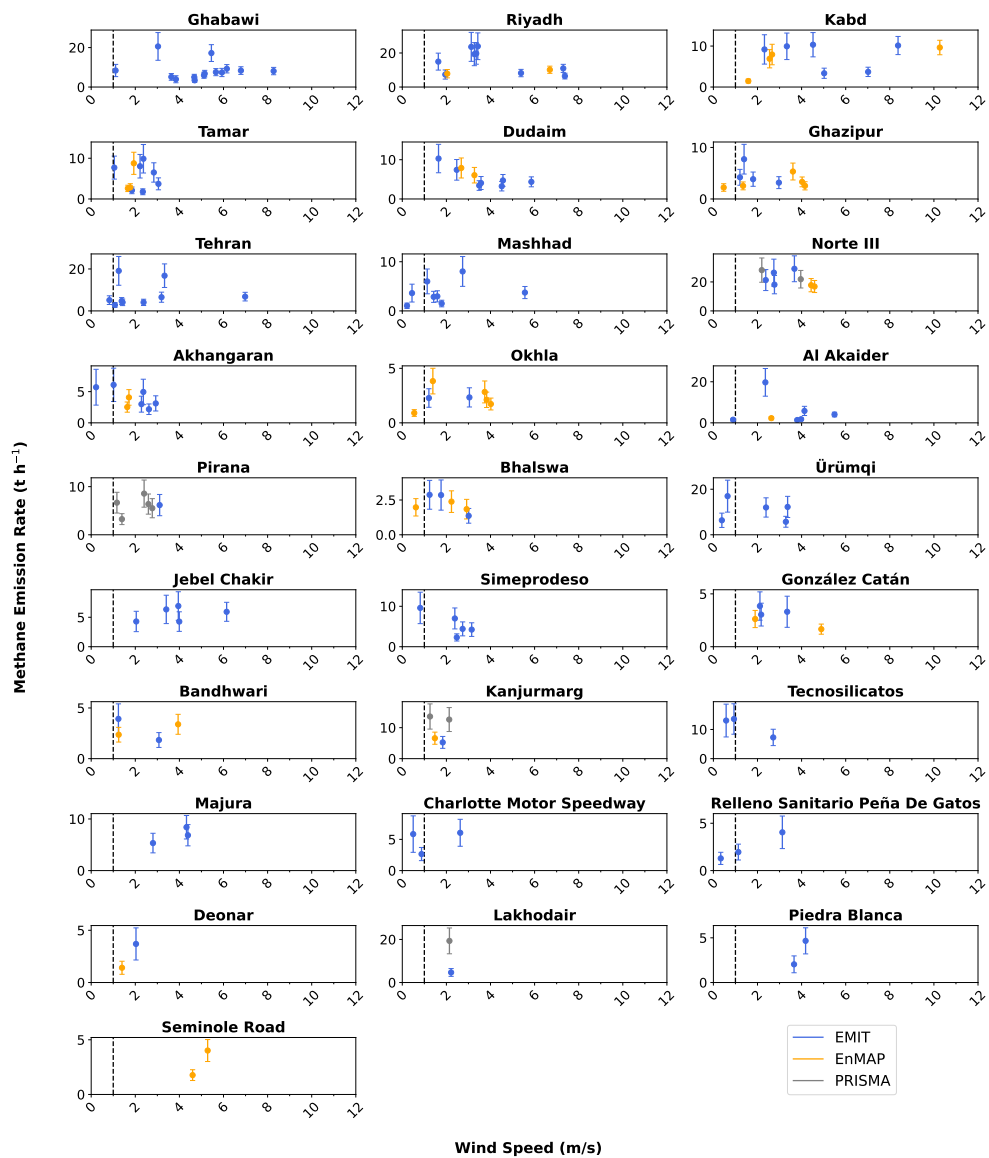


Fig. S14 Time series of methane emission rates from landfills detected at least once with HSIs.



**Fig. S15** Relationship between wind speed and methane emission rates from landfills detected at least once with HSIs.

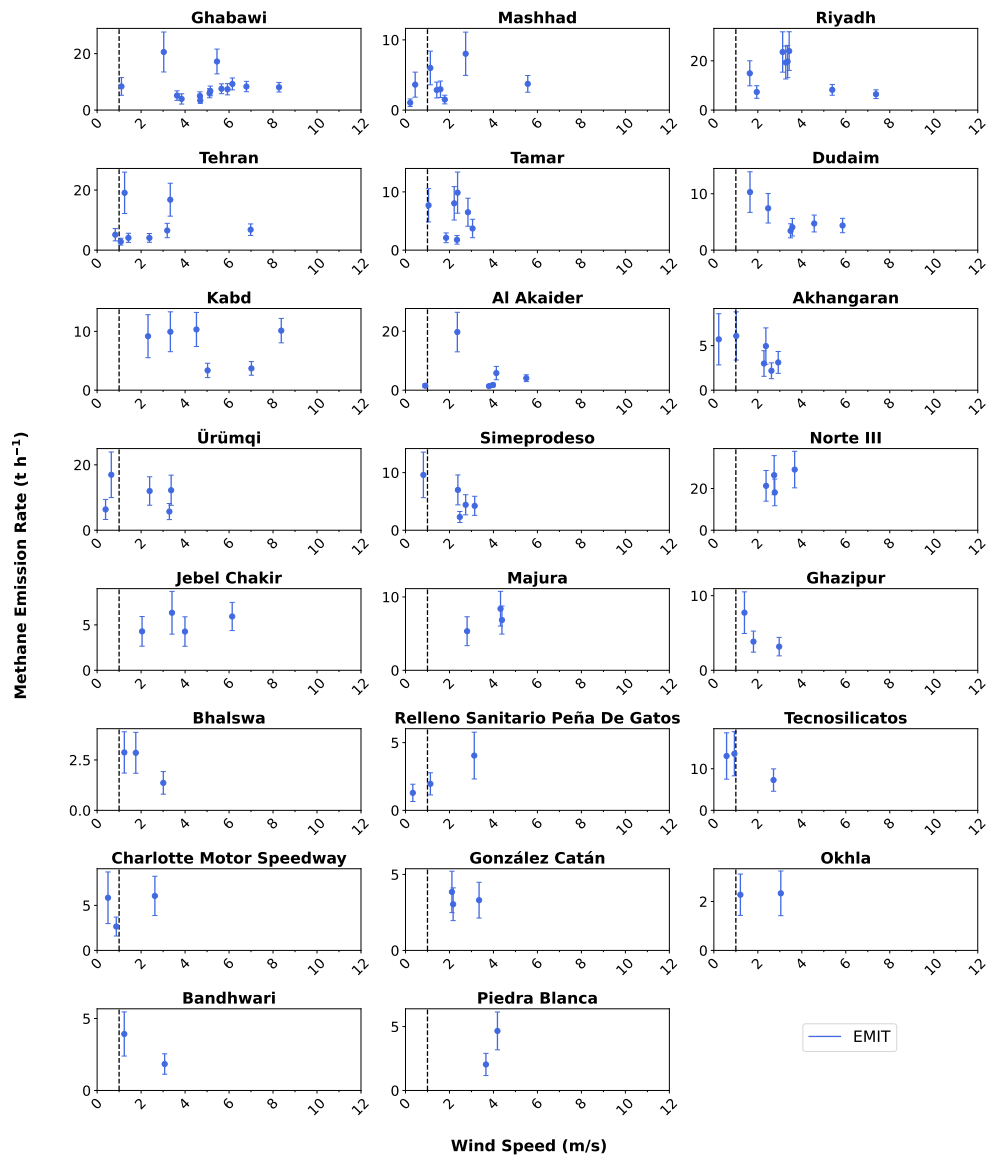
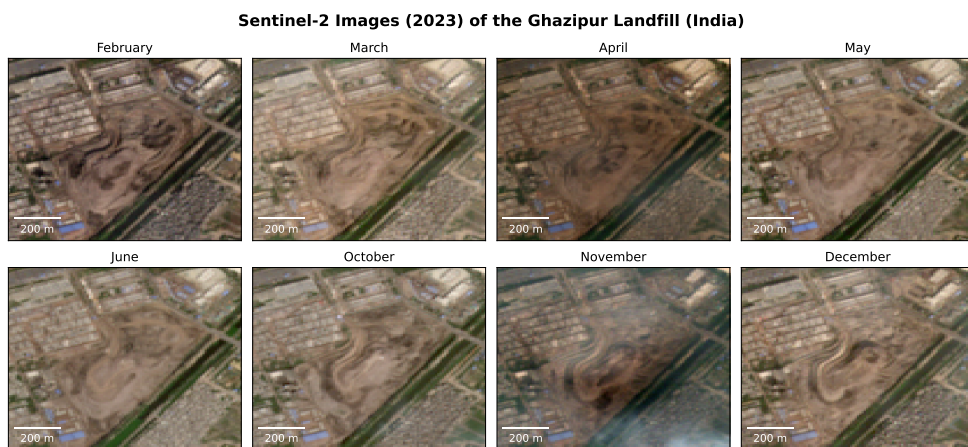


Fig. S16 Same as Fig. S15, but showing emission estimates derived from EMIT data using the IME-fetch method.



**Fig. S17** Monthly Sentinel-2 RGB images [12] captured in 2023 showing the Ghabawi Landfill in Jordan. The two white rectangles highlight two cells within the recently developed southern section. Movie S1 shows a time-lapse sequence of all cloud-free Sentinel-2 RGB images captured throughout 2023.



**Fig. S18** Monthly Sentinel-2 RGB images [12] captured in 2023 showing the Ghazipur Landfill in India. Movie S2 shows a time-lapse sequence of all cloud-free Sentinel-2 RGB images captured throughout 2023.

**Table S1** Methane emission rates for HSI measured landfills.

Country	Landfill Name	Latitude	Longitude	Plume Counts	Null Detections	Emission ( $t\ h^{-1}$ )	Uncertainty (%)
Argentina	González Catán	-34.7849	-58.6665	5	-	$2.8 \pm 0.9$	34.1
Argentina	Norte III	-34.5272	-58.6259	8	-	$22.0 \pm 6.4$	29.2
Argentina	Piedra Blanca	-31.5198	-64.2354	2	-	$3.3 \pm 1.3$	38.8
Bangladesh	Aminbazar	23.7979	90.2988	1	-	$4.1 \pm 1.6$	39.8
Brazil	Caieiras	-23.3467	-46.772	1	-	$14.0 \pm 4.8$	34.3
Brazil	Pedreira	-23.4037	-46.5608	1	-	$11.5 \pm 4.0$	34.7
China	Ürümqi	44.0384	87.8651	5	-	$10.7 \pm 4.4$	41.2
India	Bandhwari	28.4021	77.1717	4	1	$2.4 \pm 0.8$	34.3
India	Bhalswa	28.7418	77.1565	6	-	$2.2 \pm 0.8$	35.9
India	Deonar	19.0727	72.9285	2	1	$2.2 \pm 0.9$	42.9
India	Ghazipur	28.6237	77.3277	9	-	$4.0 \pm 1.3$	33.7
India	Kachara	18.6589	73.8558	1	-	$3.8 \pm 1.5$	41.0
India	Kanjurmarg	19.1233	72.952	4	-	$8.3 \pm 2.7$	32.2
India	Majura	21.1089	72.8081	3	-	$6.9 \pm 2.1$	30.9
India	Mariter Wadi	18.4702	73.9537	1	-	$3.7 \pm 1.5$	39.7
India	Okhla	28.5099	77.2849	7	1	$1.9 \pm 0.7$	35.3
India	Pirana	22.9824	72.569	6	-	$6.1 \pm 2.1$	34.8
Iran	Mashhad	36.2392	59.9882	8	-	$3.7 \pm 1.6$	42.2
Iran	Tehran	35.4585	51.3302	9	-	$7.8 \pm 2.8$	36.5
Israel	Dudaim	31.3217	34.7392	9	-	$6.2 \pm 2.1$	33.7
Israel	Tamar	31.1329	35.2013	10	-	$5.2 \pm 1.8$	34.4
Jordan	Al Akaidir	32.5143	36.1101	7	1	$3.6 \pm 1.3$	34.9
Jordan	Ghabawi	31.9302	36.1888	14	-	$8.4 \pm 2.4$	28.9
Kuwait	Kabd	29.1634	47.9138	10	-	$7.1 \pm 2.1$	30.1
Mexico	Relleno Sanitario Bicentenario	19.6512	-99.2788	1	-	$2.4 \pm 1.0$	40.6
Mexico	Relleno Sanitario Peña De Gatos	19.4031	-98.8422	3	-	$2.4 \pm 1.1$	45.0
Mexico	Simeprodoso	25.8712	-100.2993	5	-	$5.5 \pm 2.2$	39.0
Mexico	Tecnosilicatos	19.3241	-98.8033	3	-	$11.3 \pm 4.5$	40.0
Mexico	Zumpango	19.7954	-99.01	1	-	$2.1 \pm 0.9$	44.2
Pakistan	Jam Chakro	25.027	67.0359	1	-	$5.2 \pm 1.9$	35.9
Pakistan	Lakhodair	31.6248	74.4176	2	-	$12.0 \pm 4.2$	34.8
Saudi Arabia	Riyadh	24.6155	46.8953	11	-	$12.0 \pm 3.4$	28.5
Spain	Pinto	40.2636	-3.6316	1	-	$7.1 \pm 2.5$	35.0
Tunisia	Jebel Chakir	36.7371	10.0775	5	-	$5.5 \pm 2.0$	35.9
United States	Charlotte Motor Speedway	35.3405	-80.6579	3	-	$4.9 \pm 2.0$	41.8
United States	Seminole Road	33.6621	-84.257	2	-	$2.9 \pm 0.8$	26.5
Uzbekistan	Akhangan	41.0967	69.4838	8	-	$3.7 \pm 1.4$	37.1
Yemen	Al-Azraqin	15.477	44.1545	1	1	$0.6 \pm 0.2$	33.2

\*Null Detections\* refers to cases where EnMAP or EMIT has clear-sky overpasses but no plume is detected.



**Table S2** Methane emission rates aggregated by country.

Country	Emission (t h <sup>-1</sup> )	Uncertainty (%)
Argentina	28.1 ± 6.6	23.6
Bangladesh	4.1 ± 1.6	39.8
Brazil	25.6 ± 6.3	24.5
China	10.7 ± 4.4	41.2
India	41.4 ± 5.0	12.1
Iran	11.5 ± 3.2	28.2
Israel	11.4 ± 2.7	24.1
Jordan	11.9 ± 2.7	22.8
Kuwait	7.1 ± 2.1	30.1
Mexico	23.7 ± 5.3	22.3
Pakistan	17.2 ± 4.6	26.6
Saudi Arabia	12.0 ± 3.4	28.5
Spain	7.1 ± 2.5	35.0
Tunisia	5.5 ± 2.0	35.9
United States	7.7 ± 2.2	28.0
Uzbekistan	3.7 ± 1.4	37.1
Yemen	0.6 ± 0.2	33.2

Total of HSI landfill emissions in Table S1 by country. The uncertainties on average emissions for individual landfills within a country are assumed to be independent and are combined in quadrature (square root of the sum of squared uncertainties) to obtain the overall uncertainty for that country.

**Table S3** Comparison of landfill methane emission rates between HSI estimates and observational estimates (OBS) from previous studies.

Country	Landfill Name	Latitude	Longitude	HSI ( $\text{t h}^{-1}$ )	OBS ( $\text{t h}^{-1}$ )	HSI Year	OBS Report Year	OBS Source
Argentina	Norte III	-34.5291	-58.6222	$22.0 \pm 6.4$	$21.9 \pm 7.8$	2022, 2023	2021	GHGSat [3]
India	Ghazipur	28.6238	77.3278	$4.0 \pm 1.3$	$1.6 \pm 1.1$	2022, 2023	2021	GHGSat [3]
India	Kanjurmarg	19.1232	72.9535	$8.3 \pm 2.7$	$6.4 \pm 4.0$	2020, 2021, 2023	2021	GHGSat [3]
Iran	Tehran	35.4587	51.33	$7.1 \pm 2.8$	$5.0 \pm 1.0$	2022, 2023	2022	EMIT [13]
Pakistan	Lakhodair	31.6257	74.4179	$12.0 \pm 4.2$	$7.1 \pm 3.1$	2022, 2023	2020	GHGSat [3]
Spain	Pinto	40.259	-3.6357	$7.1 \pm 2.5$	$6.6 \pm 0.9$	2023	2018	In-situ [14]
United States	Charlotte Motor Speedway	35.3393	-80.6585	$4.9 \pm 2.0$	$2.9 \pm 1.0$	2023	2022	AVIRIS-NG [15]
United States	Seminole Road	33.6623	-84.2577	$2.9 \pm 0.8$	$2.9 \pm 1.1$	2023	2022	ASU GAO [15]

**Table S4** Comparison of landfill methane emission rates between HSI and the Climate TRACE inventory.

Country	Landfill Name	HSI ( $t\ h^{-1}$ )	Climate TRACE ( $t\ h^{-1}$ )	Climate TRACE Report Source	Climate TRACE Report Year
Argentina	González Catán	$2.8 \pm 0.9$	2.2	Waste Atlas	2013
Argentina	Norte III	$22.0 \pm 6.4$	3.3	Waste Atlas	2013
Argentina	Piedra Blanca	$3.3 \pm 1.3$	1.7	METER/OSM	2022
Bangladesh	Aminbazar	$4.1 \pm 1.6$	1.5	METER/OSM	2022
India	Bandhwari	$2.4 \pm 0.8$	0.02	Global Plastic Watch	2021
India	Bhalswa	$2.2 \pm 0.8$	1.4	Waste Atlas	2013
India	Deonar	$2.2 \pm 0.9$	2.4	Waste Atlas	2013
India	Ghazipur	$4.0 \pm 1.3$	2.0	Waste Atlas	2013
India	Kachara	$3.8 \pm 1.5$	0.3	Global Plastic Watch	2021
India	Kanjurmarg	$8.3 \pm 2.7$	0.4	Global Plastic Watch	2021
India	Majura	$6.9 \pm 2.1$	0.2	Global Plastic Watch	2021
India	Manter Wadi	$3.7 \pm 1.5$	0.3	Global Plastic Watch	2021
India	Okhla	$1.9 \pm 0.7$	1.9	METER/OSM	2022
India	Pirana	$6.1 \pm 2.1$	2.2	Waste Atlas	2013
Iran	Tehran	$7.8 \pm 2.8$	20.5	Waste Atlas	2013
Jordan	Al Akaidar	$3.6 \pm 1.3$	1.6	Waste Atlas	2013
Jordan	Ghabawi	$8.4 \pm 2.4$	7.3	Waste Atlas	2013
Kuwait	Kabd	$7.1 \pm 2.1$	1.5	METER/OSM	2022
Mexico	Relleno Sanitario Bicentenario	$2.4 \pm 1.0$	1.3	MEX INEGI	2016
Mexico	Simeprodeso	$5.5 \pm 2.2$	17.9	MEX INEGI	2022
Pakistan	Jam Chakro	$5.2 \pm 1.9$	2.0	Waste Atlas	2013
Saudi Arabia	Riyadh	$12.0 \pm 3.4$	1.9	METER/OSM	2022
Spain	Pinto	$7.1 \pm 2.5$	1.6	E-PRTR	2021
United States	Charlotte Motor Speedway	$4.9 \pm 2.0$	0.7	EPA GHGRP	2021
United States	Seminole Road	$2.9 \pm 0.8$	1.4	EPA GHGRP	2021
Yemen	Al-Azraqin	$0.6 \pm 0.2$	1.0	METER/OSM	2022

**Table S5** Comparison of HSI emission rates and observational estimates (OBS) from previous studies with Climate TRACE inventory for the top 20 highest emitting landfills from Climate TRACE.

Country	Landfill Name	Latitude	Longitude	Climate TRACE (t h <sup>-1</sup> )	HSI (t h <sup>-1</sup> )	OBS (t h <sup>-1</sup> )	OBS Source
Iran	Tehran	35.4585	51.3302	20.5	7.8 ± 2.8	5.0 ± 1.0	EMIT [13]
Mexico	Simeprodeso	25.8712	-100.2993	17.9	5.5 ± 2.2	-	-
Chile	Loma Los Colorados	-32.957	-70.7962	11.8	10.7 ± 3.9	1.2 ± 0.3	AVIRIS-NG [15]
Mexico	Los Laureles	20.5461	-103.1751	11.8	3.4 ± 1.4	-	-
Greece	Fyli	38.0748	23.6489	10.2	5.3 ± 2.6	-	-
Mexico	Relleno Sanitario Portezuelos	32.4073	-116.7459	9.3	6.9 ± 2.4	-	-
China	West New Territories	22.4193	113.9329	8.6	7.7 ± 2.7	-	-
Mexico	Relleno Sanitario Puebla	18.9827	-98.1368	7.8	1.7 ± 0.7	-	-
Jordan	Ghabawi	31.9302	36.1888	7.3	8.4 ± 2.4	-	-

**Table S6** Comparison of landfill methane emission rates estimated using HSI and the city-level WasteMAP inventory.

Country	City	Landfills	WasteMAP ( $t h^{-1}$ )	HSI ( $t h^{-1}$ )	HSI WasteMAP
Argentina	Buenos Aires	Norte III (8), González Catán (5)	3.8	24.8 ± 6.5	6.5
Bangladesh	Dhaka	Aminbazar (1)	3.9	4.1 ± 1.6	1.1
Brazil	São Paulo	Caieiras (1), Pedreira (1)	9.8	25.6 ± 6.3	2.6
Iran	Tehran	Tehran (9)	1.9	7.8 ± 2.8	4.1
Jordan	Amman	Ghabawi (14)	1.1	8.4 ± 2.4	7.6
Kuwait	Kuwait City	Kabd (10)	10.0	7.1 ± 2.1	0.7
Mexico	Mexico City	Zumpango (1), Relleno Sanitario Peña De Gatos (3) Relleno Sanitario Bicentenario (1), Tecnosilicatos (3)	12.5	18.2 ± 4.8	1.5
Mexico	Monterrey	Simeprodeso (5)	0.3	5.5 ± 2.2	16.3
Pakistan	Lahore	Lakhodair (2)	6.0	12.0 ± 4.2	2.0
Pakistan	Karachi	Jam Chakro (1)	5.3	5.2 ± 1.9	1.0
Saudi Arabia	Riyadh	Riyadh (11)	11.8	12.0 ± 3.4	1.0
Spain	Madrid	Pinto (1)	0.3	7.1 ± 2.5	26.8
Tunisia	Tunis	Jebel Chakir (5)	0.3	5.5 ± 2.0	18.2
Uzbekistan	Tashkent	Akhangan (8)	0.9	3.7 ± 1.4	4.0
Yemen	Sanaa	Al-Azraqin (1)	1.6	0.6 ± 0.2	0.4

The HSI emission estimates account for the cumulative methane emissions from individual landfills within each city. There can be additional waste facilities within the city with emissions not observed by the HSI. The numbers in brackets following each landfill name represent the number of detected plumes.

**Table S7** Comparison of landfill methane emission rates estimated using HSI and the country-level Climate TRACE inventory.

Country	Climate TRACE (t h <sup>-1</sup> )	HSI (t h <sup>-1</sup> )	$\frac{\text{HSI}}{\text{Climate TRACE}}$ (%)
Argentina	60.3	30.9 ± 6.7	51.3
Bangladesh	24.5	8.2 ± 2.3	33.4
Brazil	247.8	51.1 ± 8.8	20.6
China	681.5	10.7 ± 4.4	1.6
India	108.9	41.4 ± 5.0	38.0
Iran	41.5	19.3 ± 4.3	46.5
Israel	22.4	11.4 ± 2.7	50.8
Jordan	16.0	20.3 ± 3.6	127.0
Kuwait	36.7	14.3 ± 3.0	38.9
Mexico	476.6	47.4 ± 7.5	10.0
Pakistan	55.3	34.5 ± 6.5	62.4
Saudi Arabia	59.4	23.9 ± 4.8	40.3
Spain	52.5	14.3 ± 3.5	27.2
Tunisia	10.3	11.1 ± 2.8	107.2
United States	690.4	7.7 ± 2.2	1.1
Uzbekistan	21.1	7.5 ± 2.0	35.5
Yemen	11.3	1.2 ± 0.3	10.3

The HSI estimation accounts for the cumulative methane emissions from individual landfills within each country. There can be additional landfills within each country with emissions not observed by the HSI analysis presented here.

125 **Movie S1. Time-series of Sentinel-2 RGB images in 2023 for the**  
126 **Ghabawi landfill.**

127 **Movie S2. Time-series of Sentinel-2 RGB images in 2023 for the**  
128 **Ghazipur landfill.**

## 129 **References**

- 130 [1] Varon, D. J. *et al.* Satellite Discovery of Anomalously Large Methane Point  
131 Sources From Oil/Gas Production. *Geophys. Res. Lett.* **46**, 13507–13516 (2019).
- 132 [2] Varon, D. J., Jacob, D. J., Jervis, D. & McKeever, J. Quantifying Time-Averaged  
133 Methane Emissions from Individual Coal Mine Vents with GHGSat-D Satellite  
134 Observations. *Environ. Sci. Technol.* **54**, 10246–10253 (2020).
- 135 [3] Maasackers, J. D. *et al.* Using satellites to uncover large methane emissions from  
136 landfills. *Sci. Adv.* **8**, eabn9683 (2022).
- 137 [4] Varon, D. J. *et al.* Quantifying methane point sources from fine-scale satellite  
138 observations of atmospheric methane plumes. *Atmos. Meas. Tech.* **11**, 5673–5686  
139 (2018).
- 140 [5] Sherwin, E. D. *et al.* Single-blind validation of space-based point-source detection  
141 and quantification of onshore methane emissions. *Sci. Rep.* **13**, 3836 (2023).
- 142 [6] Sherwin, E. D. *et al.* Single-blind test of nine methane-sensing satellite systems  
143 from three continents. *Atmos. Meas. Tech.* **17**, 765–782 (2024).
- 144 [7] Esri, Maxar, Geographics, E. & the GIS User Community. ESRI World Imagery.  
145 [https://services.arcgisonline.com/ArcGIS/rest/services/World\\_Imagery/MapServer](https://services.arcgisonline.com/ArcGIS/rest/services/World_Imagery/MapServer)  
146 (2022).

- 147 [8] Heikenfeld, M. *et al.* Tobac 1.2: Towards a flexible framework for tracking and  
148 analysis of clouds in diverse datasets. *Geosci. Model Dev.* **12**, 4551–4570 (2019).
- 149 [9] Zhang, X. *et al.* Spaceborne Observations of Lightning NO<sub>2</sub> in the Arctic.  
150 *Environ. Sci. Technol.* **57**, 2322–2332 (2023).
- 151 [10] Jacob, D. J. *et al.* Satellite observations of atmospheric methane and their value  
152 for quantifying methane emissions. *Atmos. Chem. Phys.* **16**, 14371–14396 (2016).
- 153 [11] MacLean, J.-P. W. *et al.* Offshore methane detection and quantification from  
154 space using sun glint measurements with the GHGSat constellation. *Atmos. Meas.*  
155 *Tech.* **17**, 863–874 (2024).
- 156 [12] Sentinel-2 Cloud-Optimized GeoTIFFs. [https://registry.opendata.aws/sentinel-](https://registry.opendata.aws/sentinel-2-l2a-cogs/)  
157 [2-l2a-cogs/](https://registry.opendata.aws/sentinel-2-l2a-cogs/) (2024).
- 158 [13] Thorpe, A. K. *et al.* Attribution of individual methane and carbon dioxide  
159 emission sources using EMIT observations from space. *Sci. Adv.* **9**, eadh2391  
160 (2023).
- 161 [14] Tu, Q. *et al.* Quantification of CH<sub>4</sub> emissions from waste disposal sites near  
162 the city of Madrid using ground- and space-based observations of COCCON,  
163 TROPOMI and IASI. *Atmos. Chem. Phys.* **22**, 295–317 (2022).
- 164 [15] Carbon Mapper data. Retrieved from <https://data.carbonmapper.org> (2024).